Modelling bio-physical interactions by tube building worms.

Bachelor assignment
Jelmar Schellingerhout, 28 July 2012
Advanced Technology, University of Twente, The Netherlands

Composition research group

Name	Position	Role	Contact information
J. Schellingerhout (Jelmar)	BSc-student	Researcher	j.schellingerhout@student.utwente.nl
B.W. Borsje (Bas)	PhD-candidate	Daily supervisor	b.w.borsje@utwente.nl
N.R. Tas (Niels)	Associate Professor	Formal supervisor	n.r.tas@ewi.utwente.nl
S.J.M.H. Hulscher (Suzanne)	Professor	Promotor Bas	s.j.m.h.hulscher@utwente.nl
T.J. Bouma (Tjeerd)	Senior Researcher	Ecological advisor	t.bouma@nioo-knaw.nl

Abstract

The objectives of this study read: (1) defining the state-of-the-art knowledge on bio-physical interactions by tube building worms on hydrodynamics, sediment dynamics and the ecological environment, (2) determining the most important processes and input parameters included in the hydrodynamic model Delft-3D, (3) calibrating the model by the recently executed flume experiments and (4) determining the sensitivity in outcome of the model for a given range in input parameters for a typical North Sea situation.

The first objective has been addressed by former studies (Bouma et al., 2007; Friedrichs and Graf; 2009; Peine et al., 2009; Friedrichs et al., 2009), which confirmed that tube building worms such as the polychaete *Lanice conchilega* can both act as stabilizers and destabilizers of bed material. The patches of tube building worms have a direct effect on the near bottom water velocities and consequently on the sediment dynamics. In extreme situations, tube building worms could cause skimming flow behaviour already at 5% area coverage (Eckman et al., 1981; Friedrichs et al., 2000). As result of the biological activity of these bioengineers, the sediment fluxes could be modified by a factor 2 and more, compared to the solely physical case (Graf and Rosenberg, 1997). Indirectly, these biotic patches could have a strong (positive) environmental impact on the structure, configuration and functioning (e.g. biodiversity) of marine ecology (Callaway, 2006; Rabaut et al., 2007; Godet et al., 2008).

The latter three objectives are addressed by measuring the hydrodynamic effects in detail in the flume as result of patches of artificial structures (thin piles) and by simulating the flume set-up and five typical North-Sea scenarios with a three-dimensional hydrodynamic model. The sensitivity analysis and the calibration of the model on the flume experiments showed that this hydrodynamic model is able to provide comparable flow patterns with the flume data: (i) deceleration within the patch, (ii) acceleration above the patch, (iii) uplift in front of the patch and (iv) acceleration in front of the patch. Both the patch density and the flow velocity increase these effects of the patch on the flow dynamics. The margin of error in the velocity profiles is realistic compared to the model discrepancies of Bouma et al. (2007).

Implementing the final calibration parameter set in the model facilitated up-scaling of flume to field conditions. Using of five different typical North-Sea scenarios provided a rough estimation about what levels of bed shear stress could be found in the field as result of the patches of tube building worms. In the most extreme situation, the bed shear stresses increases with almost 60% in front of the patch and reduced with at least 80%, compared to the case with no biological activity.

Concluding, as the model performs reasonably accurate, and given that the computing time should be minimized as much as possible, it is believed that the appropriate k-ε model should be used for modelling flow through elements. However, the quality and quantity of the data should be increased in order to get more reliable results for up-scaling flume settings to field conditions. Furthermore, more processes (e.g. wave-flow interaction and flow-sediment interaction) should be included, more scenarios tested and the model should be ran in 3D.

Table of Contents

List of symbols

Roman symbols

Symbols	Units	Meaning
B_ε	m^2 / s^4	Buoyancy term for the turbulence dissipation
B_k	m^2 / s^3	Buoyancy term for the turbulence
b	m	Bed level elevation
b^*	-	Power of transport
C	$m^{1/2} / s$	2D Chézy coefficient
C_{3D}	$m^{1/2} / s$	3D Chézy coefficient
C_D	-	Drag coefficient
C_L	-	Lift coefficient
c_l	-	Coefficient that affects the geometrical length scale
c	kg / m^3	Mass concentration
$c_{1\varepsilon}$	-	Closure coefficient
$c_{2\varepsilon}$	-	Closure coefficient
$c_{3\varepsilon}$	-	Closure coefficient
c_μ	-	Closure coefficient
c'_μ	-	Closure coefficient
c_1	-	Coefficient for scaling the TKE with the bed shear stress
D	m	Stem diameter
D_H	m^2 / s	Eddy diffusivity horizontal direction
D_V	m^2 / s	Eddy diffusivity in vertical direction
d	m	Grain diameter
F	m / s^2	Drag force of the worms against the fluid
F_D	N	Flow drag force
F_f	N	Friction force
F_g	N	Gravitation force
F_L	N	Lift force
F_u	m / s^2	Drag force by patch in x-direction
F_v	m / s^2	Drag force by patch in y-direction

F_x	m/s^2	Turbulent momentum flux in x-direction
F_y	m/s^2	Turbulent momentum flux in y-direction
f	$1/s$	Coriolis parameter (inertial frequency)
f^*	-	Friction coefficient
g	m/s^2	Gravitational acceleration
H	-	Heaviside function
h_b	m	Height of the bed form
h_{TBW}	m	Height of patch
k	m^2/s^2	Turbulent kinetic energy
k_s	m	Nikuradse equivalent roughness height
L	m	Characteristic length
l	m	Available length scale for eddies inside the patch
m	$ind.m^{-2}$	Stem density
P	kg/ms^2	Hydrostatic water pressure
P_ε	m^2/s^4	Production term in transport equation for the dissipation of turbulent kinetic energy
P_k	m^2/s^3	Production term in transport equation for turbulent kinetic energy
P_x	kg/m^2s^2	Gradient hydrostatic pressure in x-direction
P_y	kg/m^2s^2	Gradient hydrostatic pressure in y-direction
R	m	Hydraulic radius
Re	-	Reynolds-number
Re_*	-	Boundary Reynolds-number
R_{xx}	m^2/s^2	Normal stress component in x-direction (divided by fluid density)
R_{xy}	m^2/s^2	Shear stress component in xy-plane (divided by fluid density)
R_{yy}	m^2/s^2	Normal stress component in y-direction (divided by fluid density)
S	kg/m^3s	Source and sink terms per unit area
S_*	-	Dimensionless sediment-fluid parameter
S_b	m^2/s	Volumetric sediment transport vector
s	-	Relative density $(=\rho_s/\rho)$
T	m^2/s^3	Additional turbulence source, generated by the work against the worms drag force
TKE	m^2/s^2	Turbulent kinetic energy

t	s	Time
U	m/s	Bulk flow velocity
u	m/s	Flow velocity in x-direction
u_*	m/s	Friction velocity
u_{*b}	m/s	Bottom friction velocity
$u_{*,c}$	m/s	Critical friction velocity
$\bar{u}$	m/s	Mean flow velocity in x-direction
u'	m/s	Velocity fluctuations in x-direction
$\vec{u}_b$	m/s	Bottom velocity vector
v	m/s	Flow velocity in y-direction
v'	m/s	Velocity fluctuations in y-direction
w	m/s	Flow velocity in z-direction
w'	m/s	Velocity fluctuations in z-direction
w_s	m/s	particle (hindered) settling velocity in a mixture
x	m	Cartesian coordinate
y	m	Cartesian coordinate
z	m	Cartesian coordinate
z_0	m	Bed roughness length
Δz_b	m	Distance to the computational grid point closest to the bed

Greek symbols

Symbols	Units	Meaning
α	-	Coefficient used to modify u_* so that αu_* forms the characteristic flow velocity past the grain
α_p	m/s^2	Bed load transport proportional parameter
α_s	-	Bed slope correction term
ε	m^2/s^3	Turbulence dissipation
ε_ε	m^2/s^4	Dissipation of ε
ζ	m	Water level elevation
θ	-	Shields parameter
θ_c	-	Critical Shields parameter
κ	-	Von Kármán constant

Symbol	Units	Description
λ	-	Solidity of the tube building worms per unit area
μ	kg/ms^2	Dynamic viscosity
ν	m^2/s	Kinematic viscosity
ν_{3D}	m^2/s	Part of eddy viscosity due to 3D turbulence
ν_H	m^2/s	Horizontal eddy viscosity
ν_H^{back}	m^2/s	Background horizontal eddy viscosity (x - and y-direction)
ν_{mol}	m^2/s	kinematic viscosity (molecular) coefficient
ν_V	m^2/s	Vertical eddy viscosity
ν_V^{back}	m^2/s	Background vertical eddy viscosity for momentum equations (x- and y-direction)
ρ	kg/m^3	Density (sea) water
ρ_0	kg/m^3	Reference density of water
ρ_s	kg/m^3	Density (suspended) solids
σ_ε	-	Closure coefficient
σ_k	-	Closure coefficient
σ_ρ	-	Prandtl-Schmidt number
τ_0	N/m^2	Bed shear stress
τ_b	N/m^2	Bottom shear stress
$\tau_{b,c}$	N/m^2	Critical bottom shear stress
τ_{bx}	kg/ms^2	Bed shear stress in x-direction
τ_{by}	kg/ms^2	Bed shear stress in y-direction
τ_b'	N/m^2	Skin friction shear stress
τ_b''	N/m^2	Form pressure shear stress
$\vec{\tau}_{b3D}$	N/m^2	Bed shear stress vector for 3D
τ_{eff}	s	Effective turbulence time scale
τ_{geom}	s	Geometricy-imposed time scale
τ_{int}	s	Intrinsic turbulence time scale
ω'	s^{-1}	Vorticity of the turbulence-velocity vector u'

1 Introduction

1.1 Problem definition

Throughout the world coastal areas are extremely important from a lot of perspectives. On an ecological perspective, these regions form the habitat for a large diversity of organisms. On an economical point of view, these areas serve for a lot of human activities like offshore constructions, maintaining navigation channels and constructing pipelines and telecommunication cables (Borsje et al., 2009). Therefore, in planning and decision-making of coastal areas, a good understanding of sediment dynamics coastal waters (Németh et al., 2003) and knowledge on spatial and temporal distribution of macrobenthic species and thus the sediment dynamics is necessary (Borja et al., 2000).

Moreover, there is a growing interest in understanding biophysical interactions between benthos and their sedimentary environment (Borsje et al., 2009). This is because sediment dynamics are caused by complex biophysical interactions between hydrodynamics and biological activity. Macrobenthic species are, by acting as either stabilizers or destabilizers (e.g. Widdows and Brinsley, 2002), able to modify the sediment fluxes by a factor two and more, compared to the case without biological activity (Graf and Rosenberg, 1997). Protruding objects from the bed, if they are relatively so close together, could even hinder the flow to such a degree that the main body of water passes over them instead of through them. The flow skims over the tips of the elements and thereby preventing the sediment from the bed to erode (Eckman et al., 1981).

A well-known protruding object is the polychaete *Lanice conchilega*, which is a tube building worm. These suspension feeding structures can have a significant (indirect) influence on the structure and functioning of marine ecosystems (Rabaut et al., 2007), e.g. *Lanice conchilega* can have a positive influence on the biodiversity (Callaway, 2006).

For these reasons, there is an increasing need for good an understanding of the interactions between polychaete tube lawns and the hydrodynamics and sediment dynamics. Hence, the predictive power of idealized models can be very useful in managing the utilization and conservation of the seabed.

1.2 Research approach

From several recent flume studies (e.g. Friedrichs et al., 2000; Bouma et al., 2007) it has become clear that tube lawns can have both a stabilizing or destabilizing effect on the sediment dynamics, depending on the flow characteristics and the density of tube building worms. Already at low densities (expressed as percentage of area coverage) of 5% skimming flow behaviour may occur., which results in a stabilizing effect on the sediment. However, at smaller densities erosion fluxes are greatly enhanced by the destabilizing effect of the individual tubes. Up-scaling of the flume experiments to field conditions by including tube building worms in numerical model should be the main focus in future researches, according to Friedrichs et al. (2009) and Peine et al. (2009). A few known studies included small scale biological activity in a large scale morphological model (Bobertz et al., 2009; Borsje et al., 2009a,b). However, all these studies making use of simplified empirical relations between the tube density and the critical shear velocity and bed roughness length, which are only justified when studying the large scale

sediment dynamics of a whole sea such as the Baltic Sea (Bobertz et al., 2009) or the Dutch part of the North Sea (Borsje et al., 2009a,b). The main (mayor) challenge is to understand the interactions between biological activity and physical processes in a process-based way. For this understanding in a process-based way, a bottom-up approach is required, in which the interaction between rigid cylindrical structures (such as the tube building worms) on drag and turbulence should be explicitly accounted for (Bouma et al., 2007).

1.3 Objectives

The objective of this research is to determine the relevant interactions between polychaete tube lawns and physical processes in the sub-tidal environment from a 'bottom-up' approach, by including rigid cylindrical structures explicitly in a three dimensional hydrodynamic model (Delft3D-FLOW). To model is already set-up, and the aim of the B.Sc. assignment is to focus on the sensitivity of the model results with respect to a variation in model parameters. Moreover, the model will be calibrated by recently executed flume experiments. Last, there will be a research on the implementation of the macrozoobenthos on more vast ecological environments.

1.4 Research questions

1. What is the state-of-the-art knowledge on bio-physical interactions by tube building worms on hydrodynamics, sediment dynamics and the ecological environment?
2. How are the most important processes included in the Delft-3D model, and what are the important input parameters?
3. How can the model be calibrated by the recently executed flume experiments?
4. Given the range in input parameters for a typical North Sea situation, what is the sensitivity in outcome of the model?

1.5 Outline of the report

In Chapter 2, 'Background', the state-of-art knowledge on biophysical interactions by tube building worms on hydrodynamics, sediment dynamics and the ecological environment will be described. This chapter will be followed by Chapter 3, 'Model Delft3D-FLOW', in which the most important processes included in Delft3D are explained.

Next, Chapter 4 gives a sensitivity analysis on the model, given the range in input parameters for typical North Sea situations. After the sensitivity analysis, in Chapter 5 the model will be calibrated by recently executed flume experiments. In Chapter 6, 'Implementation', this will be followed by an analysis how the calibrated model performs on North Sea situations. Chapter 7 will discuss the methodology and the results. Finally, Chapter 8 will provide the conclusions and recommendation obtained from this study.

2 Background

2.1 Biogeomorphology

The term biogeomorphology is defined by Viles (1988) as the discipline that combines ecology and geomorphology. Geomorphology is the study of landforms and their formation. Ecology is the study of the relationships between biota and their environment, which is defined as factors that affect biota (Baptist, 2005). Baptist (2005) subdivides these factors in three types: abiotic, biotic and anthropogenic factors. The abiotic geomorphological processes, which are non-living (physical) processes like the tide and the grain size distribution, may affect biota and vice versa. The study at this interaction between the abiotic geomorphological and biotic processes is defined as biogeomorphology (Baptist, 2005).

The relevant geomorphological factors in aquatic systems have a great range is variety. It ranges from the bed topography, bed composition (rock, gravel, sand, silt, clay), and the transport of sediment, to factors that drive morphological processes, such as water flow and waves. The abundance of biota in geomorphological environments has great influences on these geomorphological processes in order to create, maintain or transform their own geomorphological surroundings. This is demonstrated by the influence of vegetation on the hydraulic resistance, erodibility and sedimentation, or by the influence of fauna on sediment characteristics through bioturbation and biostabilization (Baptist, 2005).

In this thesis the focus will be on the bio-physical interactions by tube building worms on the hydrodynamics and sediment dynamics. However the biogeomorphological processes involves a great range of time scales, this thesis will limit its focus to the hydrodynamic and biological time scale. In Figure 2-1 (Borsje, 2009) the different time scales of biogeomorphological processes are summarized. First of all, patches of tube building worms affect the hydrodynamics through effects on the hydraulic resistance. Secondly, patches of tube building worms affect sediment transport and morphodynamics through effects on the bed shear stress and through stabilization effects by sediment trapping and destabilization effects by and sediment erodibility (Borsje, 2009). Altogether, this leads indirectly to feedback cycles that affect the coastal morphology.

2.2 Hydrodynamics

In understanding these biogeomorphological processes, knowledge of the shear stresses is of great importance. Since the shear stress at the bottom is the driving force behind the sedimentation and erosion processes, understanding these stresses is of great value to get a clear overall picture of the influences by the bio-physical interactions (De Jong, 2005). Furthermore, horizontal shear stresses in the water column are the result of differences in momentum transport, which cause friction and thereby momentum exchange in the water flow. So, the understanding the flow patterns provides a lot of information about the shear stresses.

The effect of tube building worms on flow is generally expressed as an effect on the hydraulic roughness. Boundary layer flows of aquatic systems are predominantly turbulent (Nowell and
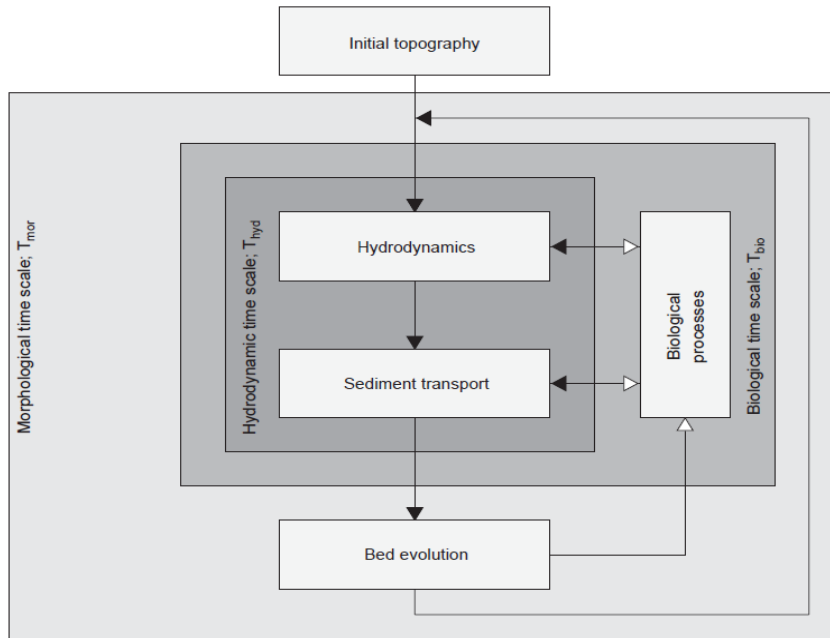
Figure 2-1 – Biogeomorphological processes divided in three different time scales (Borsje, 2009)

Jumars 1984), but viscosity plays a crucial role in the near-bed region (Friedrichs and Graf, 2009). It determines the slope of the velocity gradient through frictional retardation.

In natural systems, like the North Sea, the flow can be characterized as hydraulically rough, which means that the following logarithmic equation for the vertical velocity distribution in areas without disturbance of biota, like tube building worms, can be formulated. This vertical velocity profile has a logarithmic shape as described by the von Karman-Prandtl equation, which is often called the 'law of the wall' (Friedrichs and Graf, 2009):

$$u(z) = \frac{u_*}{\kappa} ln\left(\frac{z}{z_0}\right)$$

(1)

In this velocity formulation the term $u(z)$ is the average flow speed at a height z above a fully rough bed, κ is the empirically determined Von Kármán constant $\kappa = 0.41$. z_0 is the hydrodynamic length scale of the surface roughness, which qualitatively represents the height at which long-term average velocity equals zero. The hydraulic roughness length, z_0, in the logarithmic velocity profile was expressed by Nikuradse (1930) by Eq. 4, in which k_s is the Nikuradse equivalent roughness. The shear velocity u_* represents the steepness of the velocity gradient according to:

$$u_* = \sqrt{\frac{\tau_b}{\rho}}$$

(2)

The grain roughness for hydraulically rough flow ($\mathrm{Re}_* = \dfrac{u_* k_s}{\nu} \geq 70$, see Eq. 9) can be estimated by the White-Colebrook formulation for the Chézy value, where R is the hydraulic radius:

$$C = 18 log\left(\frac{12R}{k_s}\right) \tag{3}$$

$$z_0 = \frac{k_s}{30} \tag{4}$$

2.3 Turbulence

Turbulent, or Reynolds, stress is a common parameter describing turbulent flow conditions (Friedrichs et al., 2000). Any instantaneous horizontal flow velocity $u(z)$ can be expressed as a sum of two terms:

$$u(z) = \bar{u} + u' \tag{5}$$

where $\bar{u}$ is the mean flow velocity and u' the velocity fluctuation, which contains turbulent energy. As a measure of the magnitude of the turbulence use of the root-mean-square value $\bar{u}'$ is required. Therefore is the variance of the fluctuations denoted as $\overline{u'^2}$. Similarly to the stream wise component, the cross-channel and vertical flow component fluctuations are given by v' and w'. Altogether these fluctuations are the source of turbulent kinetic energy, which is the product of the absolute intensity of velocity fluctuations from the mean velocity (Pope et al., 2006):

$$TKE = \frac{1}{2}\rho\left(\overline{u'^2} + \overline{v'^2} + \overline{w'^2}\right) \tag{6}$$

The vertical momentum flux (Reynolds stress) is obtained from the average of the products of the fluctuations of two flow components: $-\rho\overline{u'v'}$, $-\rho\overline{u'w'}$ and $-\rho\overline{v'w'}$. The relation between the Reynolds stress and bed shear stress appears to be appropriately for fully turbulent flows with large Reynolds numbers. However, Kim et al. (2000) showed that this relation may be largely unsuitable due to tilting of the Acoustic Doppler Velocimeter (ADV, the flume measurement velocity meter) or to secondary flows. In several studies (Soulsby and Dyer, 1981; Kim et al., 2000; and Pope et al., 2006) a better relation for estimating the bed shear stress, τ_0, has been shown, namely the constant ratio of turbulent kinetic energy to shear stress:

$$\tau_0 = c_1\rho * TKE \tag{7}$$

where ρ is the sea water density and c_1 a constant value ≈ 0.2 (Kim et al., 2000 and Thompson et al., 2003). Although there are some disadvantages of this method, this approach is one of the

most robust and reliable methods to estimate the bed shear stress (Kim et al., 2000; and Thompson et al., 2003).

2.4 Energy cascade

The turbulent kinetic energy that is generated by biota, like tube building worms, is transferred into heat by viscous stresses. This transfer of turbulent energy is better known as turbulent energy dissipation (Liek, 2000). Instead of dissipation of all the turbulent kinetic energy at once, some energy remains. So the energy lost by the mean flow, due to e.g. biota, through the Reynolds stresses goes to the turbulence. According to Liek (2000), turbulence can be interpreted as the transportation mechanism from the kinetic energy of the mean flow to the dissipation into heat by means of viscous friction. This mechanism, known as the energy cascade, is described more extensively below (Figure 2-2).

As described earlier, turbulence has its origin in velocity fluctuations u'. These fluctuations tend to grow as the destabilizing centrifugal and pressure force increase the curvature (Figure 2-2). However, the viscous damping stabilizes the flow. The ratio between these destabilizing and stabilizing terms leads to the Reynolds-number (Reynolds, 1883):

$$Re = \frac{\rho \cdot u'^2/L}{\mu \cdot u'/L^2} = \frac{u'L}{\nu} \tag{8}$$

The more often so-called boundary Reynolds-number (discovered by Nikuradse) is often used to determine the properties of the flow (e.g. hydraulically rough) and the Shields parameter (see Paragraph 2.5 - Sediment dynamics):

$$Re_* = \frac{u_* k_s}{\nu} \tag{9}$$

Thus, the Reynolds-number gives in some way an interpretation how important the inertia convection terms are compared to the viscous diffusion terms. So, for more unstable flows the convection terms are more important, which results in larger Reynolds-numbers. Turbulence is thus a result of these convection terms (Veldman and Verstappen, 2001). Therefore, since Reynolds-numbers represent the intensity of turbulence, turbulent stresses are often called Reynolds stresses. These convection terms increase the frequency and decline the wavelength of the eddies by the same factor, i.e. these terms support the transfer of large-scale turbulence kinetic energy into small-scale eddies (Veldman and Verstappen, 2001). Note that this transfer is not necessarily a loss in turbulent kinetic energy. In fact, the transfer of large-scale into small-scale turbulent kinetic energy is an increase in enstrophy, which is the sum of vorticity components $\langle \omega' \cdot \omega' \rangle$ (Uittenbogaard, 2003). Here, the vorticity is the curl of the turbulence-velocity vector u', according to:

$$\omega' = \nabla * u' \tag{10}$$
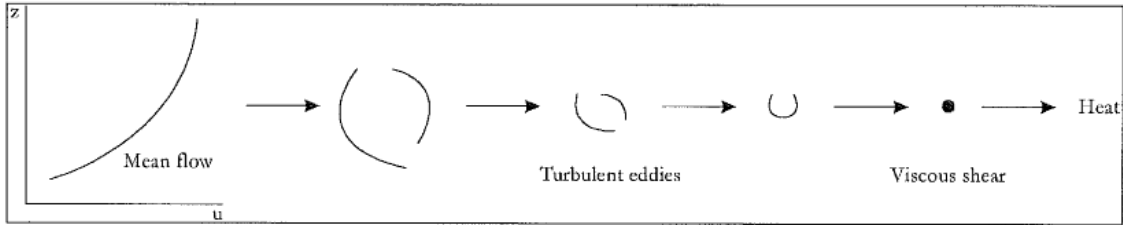
Figure 2-2 – The energy cascade of turbulence. The formed eddies transfer into smaller eddies to the point they are so small, that the viscous stresses are able to dissipate the small eddies into heat (Liek, 2000).

This cascade mechanism continues till the moment the diffusion term gets involved, i.e. till the moment the diffusion term gets sufficiently large that there is no transfer of turbulence to smaller scales anymore. Now, the smallest turbulence scale is arrived and the turbulence dissipates into heat due to viscous terms (Uittenbogaard, 2003).

2.5 Sediment dynamics

In coastal areas like the North Sea, complex phenomena of interconnected water flow and sediment transport occur (De Jong, 2005). However, sediment transport is not modelled and calculated in this report, knowledge of sediment transport is essential for understanding these morphological processes. In sediment transport there is often made a distinction between two transport mechanisms: bed load transport and suspended transport (Figure 2-3). Bed load transport is defined as the transport the transport of bed material, which rolls or jumps along the bottom (Liek, 2000). Suspended load transport is defined as the transport of material that is suspended in the water column. For the study in sediment transport several particle properties are important: size, shape, density and fall velocity (Jansen, 1994). Along with the flow properties, these sediment properties determine the sediment transport: erosion or sedimentation.

Borsje (2009) mentioned only bed load transport has to be taken into account, because Hulscher (1996) assumed this type of sediment transport is dominant in offshore tidal regimes, like the North Sea. Liu (1999) describes bed load transport as the part of the total load which has more or less continuous contact with the bed. Following this description, the bed load is related to the effective shear stress (also known as the 'skin friction shear stress') which acts directly on the grain surface:

$$\tau_b = \tau_b' + \tau_b''$$

(11)

The resistance to the flow due to the form pressure of the bed, τ_b'', is neglected, only the stress acting on single sediment due to skin friction, τ_b', is taken into account (Liu, 1999). So, for further mentions of the bed shear stress, it easily can be replaced by the effective shear stress since the shear stress from form pressure has been neglected.

If a spherical grain resting on the bed composed of cohesionless grains is considered, the forces that will act on the grain are shown in (Figure 2-3). The friction force F_f is equal to the driving force the flow drag force on the grain F_D and depends on the lift force F_L and the force as result of the submerged weight w', according to (Liu, 1999):
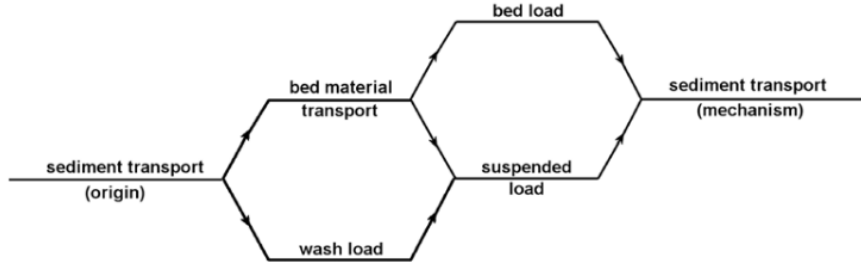
Figure 2-3 – The distinguish in the sediment transport mechanism between bed load transport and suspended load transport (De Jong, 2005).
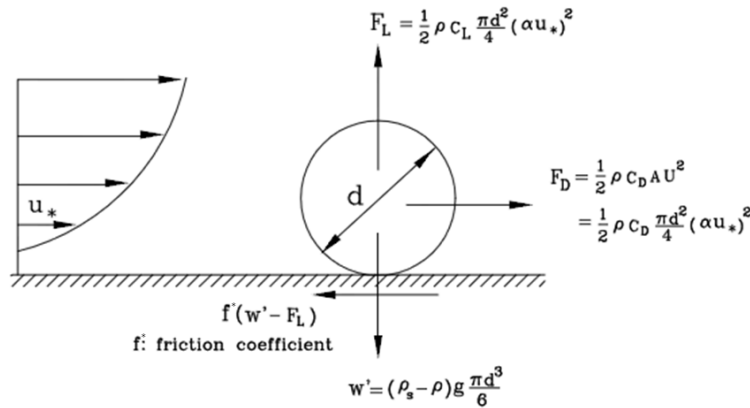
Figure 2-4 – Forces acting on a grain resting on a flat bed (Liu, 2001).

$$F_D = F_f$$

(12)

$$\frac{1}{2}\rho C_D \frac{\pi d^2}{4}(\alpha u_*)^2 = f^*(F_g - F_L) = f^*\left((\rho_s - \rho)g\frac{\pi d^3}{6} - \frac{1}{2}\rho C_L \frac{\pi d^2}{4}(\alpha u_*)^2\right)$$

(13)

This can be rearranged to:

$$\frac{u_{*,c}^2}{(s-1)gd} = \frac{f^*}{\alpha^2 C_D + f^*\alpha^2 C_L}\frac{4}{3\alpha^2}$$

(14)

Where the dimensionless Shields parameter is given by:

$$\theta = \frac{u_{*,c}^2}{(s-1)gd}$$

(15)

From this relation, the conditions when a particle starts to move are defined as:

- $u_* > u_{*,c}$ critical friction velocity $u_{*,c}$,
- $\tau_b > \tau_{b,c}$ critical bottom shear stress $\tau_{b,c} = \rho u_{*,c}^2$,
- $\theta > \theta_c$, critical Shields parameter $\theta_c = \dfrac{u_{*,c}^2}{(s-1)gd}$.

Thus, the Shields parameter is dimensionless indicator whether there occur erosion or sedimentation processes. Experimentally the critical Shields parameter has been determined to be related to the grain Reynolds number, the so called Shield diagram. However, now the friction velocity appears in both axes, so the critical Shield parameter has been related to the so-called dimensionless sediment-fluid parameter S_* (Liu, 1999):

$$S_* = \frac{d\sqrt{(s-1)gd}}{4\nu} \tag{16}$$

From this sediment-fluid parameter, the critical Shields parameter can be determined, using this diagram presented in Figure 2-5. From the critical Shields parameter the critical bed shear stress can be derived, according to:

$$\tag{17}$$
$$\tau_{b,c} = \theta_c g(s-1)\rho d$$

A lot of relations between the bed shear stress and the bed load transport have been derived by experimentally data fitting (Liu, 1999).Van der Veen et al. (2006) suggested a bio-geomorphological model (based on earlier work by Hulscher (1996)) in which the transport equation reads:

$$S_b = \alpha_p |\tau_b|^{b^*} \left(\frac{\tau_b}{|\tau_b|} - \alpha_s \nabla h_b \right) H \left(1 - \frac{\tau_{b,c}}{\tau_b} \right) \tag{18}$$

where S_b is the volumetric sediment transport vector and α_p the bed load transport proportional parameter. b^* indicates the non-linear relation of the transport and bed shear stress. α_s is a correction factor for the slope and h_b is the height of the bed form. As last, H is the Heaviside function which makes sure sediment is only transported when the above described conditions are satisfied. For a more detailed description see Borsje (2009).

2.6 Flow-element interaction

Morris (1955) classified flow over rough surfaces, like a field of tube building worms, into three categories. Isolated-roughness flow is likely to occur with sparse cover of objects protruding from the bed. The formed eddies behind each object dissipate before the next object is reached (Figure 2-6a, Figure 2-7a).

In intermediate conditions, when the roughness elements are closer together, only the tails of the mixing zone are affected (Parsons and Abrahams, 2009) (Figure 2-6b, Figure 2-7b). This interaction of elements' eddies causes intense turbulence (Gordon et al., 1992).

In skimming flow conditions, the elements are relatively so close together and hinder flow to such a degree, that the main body of water passes over them instead of through them and causing the flow to skim over the tops of the elements (Gordon et al., 1992) (Figure 2-6c, Figure 2-7c). Because low velocities occur between the elements, the surface acts as if it is hydraulically smooth (Gordon et al., 1992). Therefore, in skimming flow conditions the entire flow profile is displaced upward and thereby preventing sediment from the bed to erode (Eckman et al., 1981).

From several studies (Friedrichs et al., 2000; Bouma et al., 2007; Friedrichs and Graf, 2009; Peine et al., 2009; Friedrichs et al., 2009) we know that already at low densities (expressed as percentage of area coverage) of 5% skimming flow behaviour may occur. However, at smaller densities erosion fluxes are greatly enhanced by the destabilizing effect of the individual tubes. In summary, tube lawns can have both a stabilizing and destabilizing effect on the sediment dynamics, depending on the flow characteristics and the density of tube building worms.
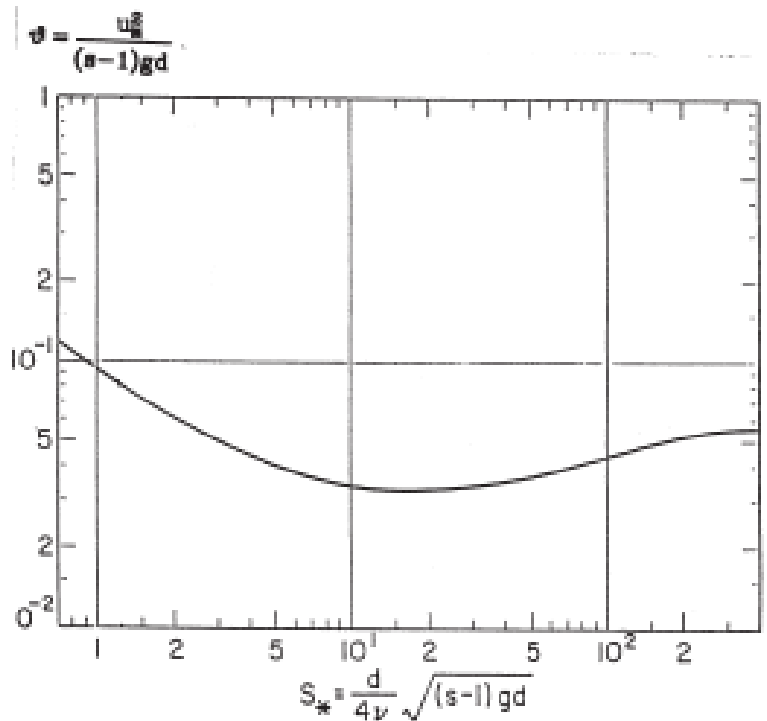
Figure 2-5 – The Shields diagram giving θ_c as function of S_* (Liu, 2001).
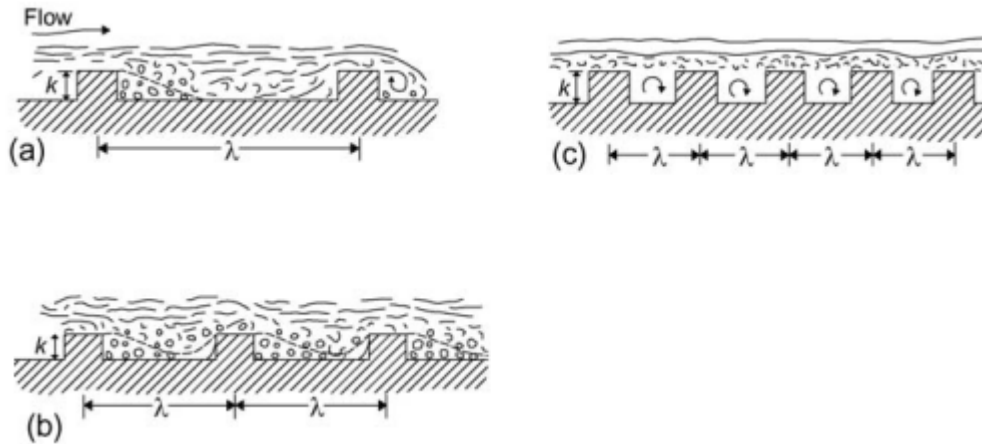
Figure 2-6 – The classification of flow near rough surfaces. Diagrammatic illustrations of the flow patterns in (a) isolated roughness flow, (b) wake-interference flow, (c) skimming flow, which are based on the classification of Morris (1955) and have been obtained from Gordon et al. (1992).
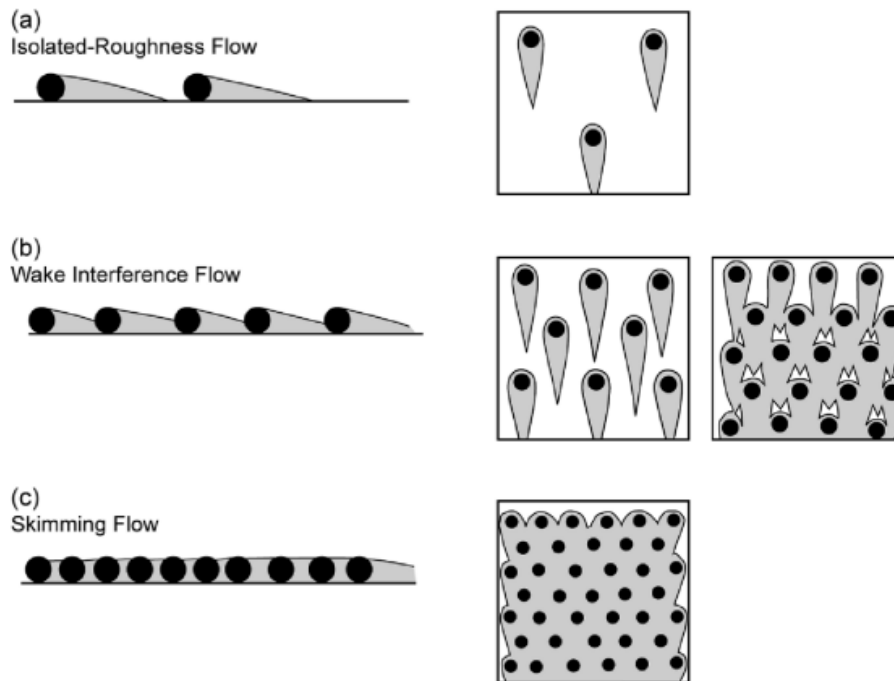
Figure 2-7 – Effects of multiple roughness elements (tube building worms) on flow profiles, where the grey area represents the wake area formed by the flow-element interaction (Parsons and Abrahams, 2009; original: Wolfe and Nickling, 1993).

3 Measurements

3.1 Flume measurements

Direct effects by tube building worms are extensively discussed in different flume studies (Friedrichs et al., 2000; Friedrichs and Graf; 2009; Peine et al., 2009; Friedrichs et al., 2009). From these studies it is known that that already at low densities of 5% skimming flow behaviour may occur. At smaller densities, however, erosion fluxes are greatly enhanced by the destabilizing effect of the individual tubes. Furthermore, the exact behaviour of the flow upstream of the patch still has to be validated by combining flume experiments with three dimensional hydrodynamic modelling. In this investigation of flow patterns, the tube building worms will be represented by rigid cylindrical structures. In the hydrodynamic modelling the rigid cylindrical structures can be implemented straightforward. In the flume measurements the worms are represented by thin straws.

It should be noted that flow in flume tanks is always at best an idealized representation of flow in the field. In general, turbulence intensities in the flume are lower than in the field and the flume tank dimensions determine the largest eddy sizes (Bouma et al., 2007). Nevertheless, former work has indicated that turbulence levels found in the NIOO flume tank are very comparable to situations of steady flow in the field (Hendriks et al., 2006).

3.2 Flume tank

All information about the flume is extensively described in reports by Bouma et al. (2005 and 2007). The most important characteristics of the flume, obtained from these reports, are described below.

The flow within the patch was characterised in a 17.5 m long flume at the NIOO laboratory in Yerseke, see Figure 3-1. The straight working section of 10.8 m has a cross section of 0.60 m wide and the water depth is maintained at 0.40 m. A conveyor belt system generates flow velocities up to 0.45 ms^{-1} and has a total capacity of 9 m^3. In order to get laminar flow at the beginning of the working section, the water passes through several tubes (Ø 20 mm) which act as collimators. The 2 m long test section (Figure 3-2), located at the downstream end of the working section, has an adjustable bottom that allows the placement of sediment and the same bottom level of the working section and the test section. In this test section an Acoustic Doppler Velocimeter (ADV), which was positioned by a computerised 3D system, measures the flow velocity in all three directions. During the flow measurements, small amounts of suspended solids were added in order to facilitate the velocity measurements of the ADV. This suspended solids stay in suspension at even very low velocities and have no significant influence on the measurement results.

3.3 Flume experiment set-up

First of all, a patch is created on the height-adjustable bottom, which contains a representative sediment of the sediment found in the field. The patch has a length of 50 cm and a width of 60 cm. All the thin straws are placed in the sediment such that the height is 3.5 cm.

Experiment settings	
Water level	0.4 m
Bulk flow velocity	[0.1 0.2] ms^{-1}
Patch density	[1632 2448 3264] individuals.m^{-2}
Diameter TBW	0.5 cm
Height TBW	3.5 cm
X-position	[90:-5:-5] cm
Y-position	[0] cm
Z-position	[0.5 1 2 3 4 5 6 8 10 15 20 31] cm
Measurement time per location	5 min
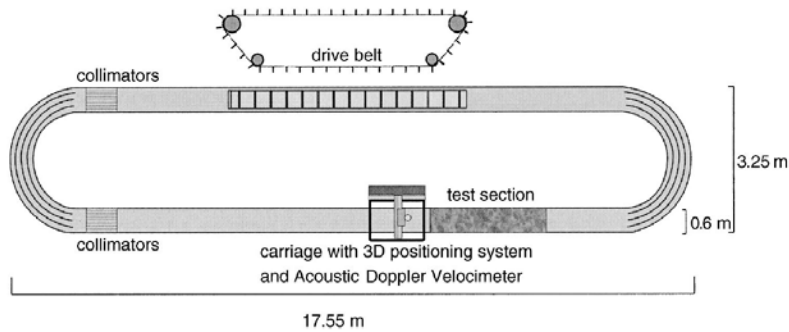
Figure 3-1 – The flume tank (side-view) used for the experiments (Bouma et al., 2005).
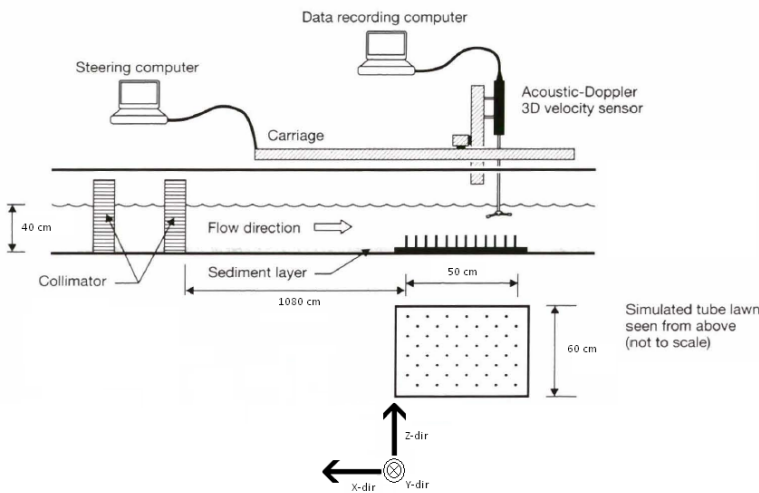
Figure 3-2 – The working section and test section of the flume tank (side-view), including the steering computer, ADV and patch of tube building worms (Friedrichs et al., 2000). Note that the sizes and distances are adjusted in such a way it corresponds with those of Figure 3-1.
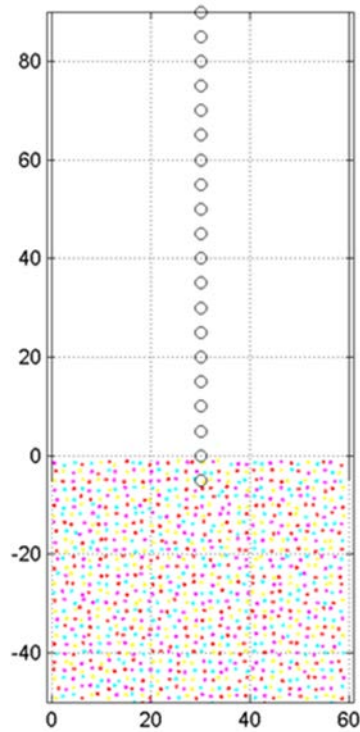
Figure 3-3 – A top view of the flume tank with the measurement locations in the x-direction. The patch of tube building worms is indicated by dots with different colours, which are used to facilitate the execution of the different experiment settings (Borsje et al., 2011).
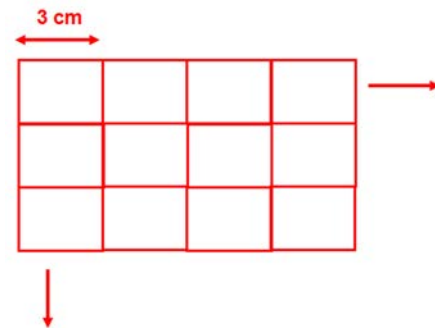
Figure 3-4 – The constructed grid which was used to place the thin straws in a randomly and evenly distributed way (Borsje et al., 2011).

Note that the width of the patch fills up the whole width of the flume tank. Thus, in this way, only flow over the patch is simulated. Although this is not a realistic representation of the field circumstances, it facilitates the focus on the research parameters since this assumption simplifies the model a lot.

In order to distribute the thin piles randomly, over the test section, a grid was constructed (see Figure 3-4). Each "grid cell" represents a small area, over which a small number of thin piles could be placed. The number of piles placed into the grid cells was fixed for each experiment setting. Between the different experiment settings the fixed number of thin piles per cell could vary from one to four. In order to facilitate and to speed up the experiments, all piles within a cell have different colours which are the same for all cells (Figure 3-3). In this way, one colour of piles can be removed (or placed) in order to produce three different realistic patch densities.

Beside different patch densities, different bulk flow velocities influence the flow patterns around and within the patch (and thus the sediment dynamics). Therefore, for each patch density, two different realistic bulk flow velocities (0.1 and 0.2 ms^{-1}) are used.

The influences of the different patch densities and bulk flow velocities on the velocity profiles is measured on different locations in the flow direction and in the vertical direction, i.e. the x-direction and the z-direction respectively. The measurement positions on the x-direction are located every 5 cm, starting at 90 cm upstream of the patch till 5 cm within the patch. The

measurement positions on the z-direction near the bottom are located every centimetre, starting at the bottom. Above 10 cm the velocity profile is significantly less influenced by the patch than below 10 cm, less measurement points are sufficient to obtain realistic velocity profiles (Table 3-1). For the measurement locations in the y-direction only one location is used, viz. exactly in the middle of the flume thank. Since there are no variations in the y-direction, it is valid to use only one measurement location, which reduces the measurement time a lot. It should be mentioned that it is assumed that walls of the flume tank have no significant influence on the velocity profiles in the middle of the flume tank. At every location all three velocity components (x-, y- and z-direction) are measured with the ADV for 5 minutes, i.e. each measurement setting lasts for 20 hours.

4 Model Delft3D-FLOW

4.1 Introduction

In this study, the three-dimensional hydrodynamic model Delft3D is used. The Delft3D package, developed by Deltares (former WL|Delft Hydraulics) is a model system that consists of a number of integrated modules which together allow the simulation of hydrodynamic flow (under the shallow water assumption), computation of the transport of water-borne constituents (e.g., salinity and heat), short wave generation and propagation, sediment transport and morphological changes, and the modelling of ecological processes and water quality parameters (Lesser et al., 2004).

Here only the FLOW-module will be used, so all interactions by waves are neglected. The Delft3D-FLOW module computes flow characteristics (flow velocity, turbulence) dynamically in time over a three-dimensional spatial grid. By the many processes included in the module, Delft3D-FLOW is capable of 3D simulations of ocean basins, coastal seas and rivers, etc. (Lesser, 2004).

Below a brief description of the model is given. A full mathematical description is given by Deltares (2009). In the first section the governing equations used in Delft3D-FLOW are discussed, followed by their numerical implementation in the second section. In the last section the model setup used in this study is described.

4.2 Governing equations

4.2.1 Hydrodynamic and transport equations

The Delft3D-FLOW module, extensively described by Lesser et al. (2004), uses a set of equations, consisting of the horizontal momentum equations, the continuity equation, the transport equation, and a turbulence closure model. Delft3D-FLOW solves the Navier-Stokes equations for an incompressible fluid, under the shallow water and the Boussinesq assumptions. The boundary conditions used to solve the following equations are described in Appendix 2.

The used Cartesian coordinate system by Delft3D has a transformed vertical coordinate (Figure 4-1). However, in this study a flat bed is modelled, so there is no need for a transformation to the vertical σ-coordinate system and so the equations are described for a "normal" Cartesian coordinate system *(x, y, z, t)*. The *x*-, *y*- and *z*-axis are orientated to the north, east and upward away from the bed respectively. The *z*-axis ranges from *-d(x, y)* at the bed, to *ζ(x, y, t)* at the free surface where *d* = 0.

Because vertical accelerations can be neglected, also known as that "shallow water assumption", the vertical momentum equation reduces to the hydrostatic pressure equation:

$$\frac{\partial P}{\partial z} = -\rho g \ .$$

(19)

The continuity and momentum equations in *x* and *y* direction are respectively given by,
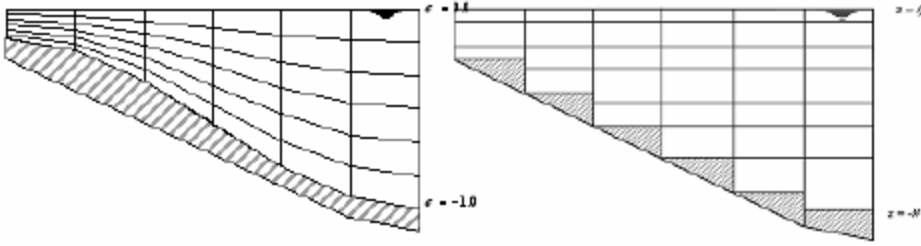
Figure 4-1 – Example of σ-grid and z-grid used in Delft3D. In this thesis the z-grid has been used (Deltares, 2009).

$$\frac{\partial u}{\partial x} + \frac{\partial v}{\partial y} + \frac{\partial w}{\partial z} = 0 \,, \tag{20}$$

$$\frac{\partial u}{\partial t} + \frac{\partial u^2}{\partial x} + \frac{\partial uv}{\partial y} + \frac{\partial uw}{\partial z} - fv + \frac{1}{\rho_0} P_x - F_x - \frac{\partial}{\partial z}\left(\nu_V \frac{\partial u}{\partial z}\right) = 0 \,, \tag{21}$$

$$\frac{\partial v}{\partial t} + \frac{\partial vu}{\partial x} + \frac{\partial v^2}{\partial y} + \frac{\partial vw}{\partial z} + fu + \frac{1}{\rho_0} P_y - F_y - \frac{\partial}{\partial z}\left(\nu_V \frac{\partial v}{\partial z}\right) = 0 \,. \tag{22}$$

In which ν_V is the vertical turbulent eddy viscosity and the horizontal pressure terms P_x and P_y for a certain depth z can be determined by (Boussinesq approximations),

$$\frac{1}{\rho_0} P_x = g \frac{\partial \zeta}{\partial x} + \frac{g}{\rho_0} \int_z^\zeta \left(\frac{\partial \rho}{\partial x} + \frac{\partial z'}{\partial x}\frac{\partial \rho}{\partial z'}\right) dz' \,, \tag{23}$$

$$\frac{1}{\rho_0} P_y = g \frac{\partial \zeta}{\partial y} + \frac{g}{\rho_0} \int_z^\zeta \left(\frac{\partial \rho}{\partial y} + \frac{\partial z'}{\partial y}\frac{\partial \rho}{\partial z'}\right) dz' \,. \tag{24}$$

The horizontal friction terms F_x and F_y, also known as the Reynold's stresses, are determined using the eddy viscosity concept extensively described by Rodi (1984) and are given by,

$$F_x = \frac{\partial}{\partial x}\left(2\nu_H \frac{\partial u}{\partial x}\right) + \frac{\partial}{\partial y}\left(\nu_H \left(\frac{\partial u}{\partial y} + \frac{\partial v}{\partial x}\right)\right) \,, \tag{25}$$

$$F_y = \frac{\partial}{\partial y}\left(2\nu_H \frac{\partial v}{\partial y}\right) + \frac{\partial}{\partial x}\left(\nu_H \left(\frac{\partial u}{\partial y} + \frac{\partial v}{\partial x}\right)\right) \,. \tag{26}$$

In Delft3D-FLOW the transport of matter (sediment) is modelled by the advection-diffusion equation. This transport equation is used to calculate the three-dimensional transport of suspended sediment. Furthermore, the transport equation is also used for the transport of

momentum resulting in the equations for the turbulent kinetic energy k and the turbulent energy dissipation ε. The transport equation is given by,

$$\frac{\partial c}{\partial t} + \frac{\partial uc}{\partial x} + \frac{\partial vc}{\partial y} + \frac{\partial (w - w_s)c}{\partial z} = \frac{\partial}{\partial x}\left(D_H \frac{\partial c}{\partial x}\right) + \frac{\partial}{\partial y}\left(D_H \frac{\partial c}{\partial y}\right) + \frac{\partial}{\partial z}\left(D_V \frac{\partial c}{\partial z}\right) + S \quad (27)$$

.

In order to solve the equations above, the unknown horizontal and vertical diffusivity (D_H and D_V) and viscosity (ν_H and ν_V) need to be prescribed. In this study, no actual sediment transport is calculated so the diffusivity terms can be neglected. Delft3D assumes the horizontal viscosity coefficient is a superposition of three parts: a part due molecular viscosity, a part due "2D turbulence" and a part due "3D turbulence". The molecular viscosity of the water is a constant value with order of magnitude 10^{-6}. The "2D turbulence" part associated with the horizontal mixing that is not resolved by advection on the horizontal computational grid. In this study, the 2D turbulence is specified by constant parameters, the background horizontal eddy viscosity coefficient ν_H^{back}. The "3D turbulence" part is in Delft3D computed by the selected turbulence closure model (see the turbulence section below). So the horizontal viscosity coefficient becomes,

$$\nu_H = \nu_{mol} + \nu_H^{back} + \nu_{3D} \quad (28)$$

.

The vertical eddy viscosity consists also of three parts. The first part is the constant kinematic viscosity. Secondly, a background vertical eddy viscosity can be specified for taking into account the unresolved mixing. Finally, for calculating the third part, the 3D viscosity, also a turbulence closure model is used. The three parts lead to the vertical eddy viscosity by,

$$\nu_V = \nu_{mol} + \max\left(\nu_V^{back}, \nu_{3D}\right) \quad (29)$$

.

4.2.2 Turbulence

The Navier-Stokes equations for an incompressible fluid described above are capable of resolving the turbulent scales, but usually the hydrodynamic grids are too coarse and the time step too large to resolve the turbulent scales of motion in these equations (Deltares, 2009). The turbulent processes are called "sub-grid". For this reason, the basic equations are Reynolds-averaged introducing so-called Reynolds stresses (equations 25 and 26), which are related to the Reynolds-averaged flow quantities by a turbulence closure model. The turbulence closure model provides appropriate assumptions for solving the unknowns as result of filtering the equations, like:

$$\nu_V = c'_\mu L \sqrt{k} \quad (30)$$

and

$$\varepsilon = c_D \frac{k\sqrt{k}}{L}, \quad (31)$$

Combining equation 30 and 31 gives:

$$v_V = c'_\mu L \sqrt{k}$$
$$= c_\mu \frac{k^2}{\varepsilon},$$
(32)

with $c_\mu = c'_\mu c_D = 0.09$.

The first assumption provides a closure for the eddy viscosity, relating it to a characteristic length scale L and velocity scale. The velocity scale is based on the kinetic energy of turbulent motion k. c'_μ is a calibration constant determined by the closure model. The second assumption provides the relation between the energy dissipation ε the turbulent kinetic energy k, which is a function depended on the mixing length L and the calibration constant c_D.

The simplest turbulence closure model suitable for modelling the flow through vegetation is the k-ε turbulence model (Uittenbogaard, 2003). By representing tube building worms by thin piles on the bottom of the seabed, the worms can be included in a vegetation model. In this way, the influence of tube building worms on the near bottom flow can be modelled this second order turbulence closure model. One of the main advantages of the k-ε turbulence model is that stratification is taken into account by the buoyancy terms in the transport equations for k and ε (Deltares, 2009).

In the k-ε turbulence closure model both the turbulent energy k and the dissipation ε are produced by production terms representing shear stresses at the bed, surface, and in the flow (Lesser et al., 2004). The values for k and ε for every grid cell are then calculated by transport equations. The equations for the turbulent kinetic energy k and the dissipation ε, where wave interaction are neglected, are respectively given by,

$$\frac{\partial k}{\partial t} + u\frac{\partial k}{\partial x} + v\frac{\partial k}{\partial y} + w\frac{\partial k}{\partial z} = \frac{\partial}{\partial z}\left[\left(v_{mol} + \frac{v_{3D}}{\sigma_k}\right)\frac{\partial k}{\partial z}\right] + P_k + B_k - \varepsilon,$$
(33)

$$\frac{\partial \varepsilon}{\partial t} + u\frac{\partial \varepsilon}{\partial x} + v\frac{\partial \varepsilon}{\partial y} + w\frac{\partial \varepsilon}{\partial z} = \frac{\partial}{\partial z}\left[\left(v_{mol} + \frac{v_{3D}}{\sigma_\varepsilon}\right)\frac{\partial \varepsilon}{\partial z}\right] + P_\varepsilon + B_\varepsilon - \varepsilon_\varepsilon,$$
(34)

with the Prandtl-Schmidt numbers $\sigma_k = 1$ and $\sigma_\varepsilon = 1.3$. The second term in the right-hand side, P_k, represents the production of turbulent kinetic energy in shear flows (Uittenbogaard, 2003). The buoyancy flux, B_k, represents the conversion of turbulent kinetic energy into potential energy. The last three terms in the energy dissipation equation are the production term of the energy dissipation P_ε, the buoyancy flux B_k and the dissipation of the dissipation ε_ε. An more extensive description of these terms is given in Appendix 2.

4.2.3 Bed shear stress
For three dimensional models, the bed shear stress component, which is related to the current just above the bed, and the Chézy coefficient are formulated respectively by,

$$\vec{\tau}_{b_{3D}} = \frac{g\rho_0 \vec{u}_b |\vec{u}_b|}{C_{3D}^2},$$
(35)

$$C_{3D} = \frac{\sqrt{g}}{\kappa} \ln\left(1 + \frac{\Delta z_b}{2z_0}\right). \tag{36}$$

where Δz_b is the distance to the computational grid point closest to the bed.

4.3 Vegetation model

4.3.1 Extra equations

The difference with the standard version of Delft3D is the inclusion of the effect of the tube building worms on the flow and that it account explicitly for the influence of rigid cylindrical structures, like tube building worms, on the drag and turbulence. The 3D-model is a research version of Delft3D based on the same equations as defined for the 1-DV model designed by Uittenbogaard (2003). In this section only the extra source terms are described. The complete 3D-model description is given in Appendix 2.

In the 3D-model the influence of the cylindrical structures is particularly noticeable by three extra source terms (Uittenbogaard, 2003). The first extra source term is the inclusion of the friction force (the drag force), F (N/m^2), imposed on the mean flow by the tube building worms in the momentum equations:

$$F_u = \frac{1}{2}C_D m(z)d(z)u\sqrt{u^2 + v^2}, \tag{37}$$

$$F_v = \frac{1}{2}C_D m(z)d(z)v\sqrt{u^2 + v^2}, \tag{38}$$

where $d(z)$ is the stem diameter (m) and $m(z)$ is the stem density (m^{-2}). C_D is the drag coefficient (-).

The second and third extra source terms are the adjustments of the $k-\varepsilon$ equations are respectively:

$$\left(\frac{\partial k}{\partial t}\right)_{\text{cylinders}} = \frac{1}{1-\lambda(z)}\frac{\partial}{\partial z}\left((1-\lambda(z))\left(v + \frac{v_V}{\sigma_k}\right)\frac{\partial k}{\partial z}\right) + T(z), \tag{39}$$

$$\left(\frac{\partial \varepsilon}{\partial t}\right)_{\text{cylinders}} = \frac{1}{1-\lambda(z)}\frac{\partial}{\partial z}\left((1-\lambda(z))\left(v + \frac{v_V}{\sigma_\varepsilon}\right)\frac{\partial \varepsilon}{\partial z}\right) + c_{2\varepsilon}\frac{T(z)}{\tau_{eff}}, \tag{40}$$

where the horizontal cross-section area of the epibenthic structures per unit area at height z is given by:

$$\lambda(z) = \frac{\pi}{4}D(z)^2 m(z). \tag{41}$$

The term $T(z)$ (Watt/m^3) is the additional turbulence source generated by the tube building worms and represents the work spent by the fluid at a height z. This work against the worms drag force is converted into turbulent kinetic energy and, therefore, is given by:

$$T(z) = F\sqrt{u^2 + v^2}\,. \tag{42}$$

The second term in ε–equation corresponds to the dissipation rate of the turbulence produced by the worms (Uittenbogaard, 2003). The rate at which the turbulent kinetic energy produced by the worms is converted into enstrophy is given by τ_{eff}. This effective turbulence dissipation time scale is related by Uittenbogaard (2003) to different length scales that control turbulence inside the worm field (Figure 4-2). The first length scale is from the internally-generated turbulence, which is smaller than the available fluid space inside the worms. The relevant time scale of this small-scale turbulence equals to the intrinsic turbulence time scale:

$$\tau_{int} = \frac{k}{\varepsilon}\,. \tag{43}$$

However, this turbulence length scale is only valid at sufficient distance from the bed as well as from the top of the worms. The reason for this is shown by Figure 4-3, where the penetration of the shear-flow turbulence from above the worm field into the upper layer of the worms, i.e. the large eddies that are transferred from above the worms have to be squeezed into smaller-scale eddies of the available length scale (Baptist, 2005). This, geometrically determined, relevant time scale is given by,

$$\tau_{geom} = \left(\frac{l^2}{c_\mu{}^2 T}\right)^{\frac{1}{3}}, \tag{44}$$

with

$$l(z) = c_l \left(\frac{1 - \lambda(z)}{m(z)}\right)^{\frac{1}{2}}, \tag{45}$$

where c_l is a coefficient with value 0.8 (Bouma et al., 2007).

This model has been validated against laboratory flume experiments (Borsje, 2009; Bouma et al., 2007) and against field data on flow patterns in salt marshes (Temmerman et al., 2005), intertidal flats and sandy sites (Bouma et al., 2007).

4.3.2 Model set-up

In this part, to the most important model input fields is referred i.e. the grid and the open boundary conditions. Both the module in which the worms are translated to thin piles and the numerical aspects of Delft3D are described in Appendix 2.

4.3.2.1 2DV

Although the model Delft3D can run and calculate several variables in different dimensions, sometimes it is not necessary to run it in 3D. By simulating certain settings in fewer dimensions, the costly calculation-time can be reduced whereas the model output can still contain sufficient information. A schematized two-dimensional vertical (2DV) model (Figure 4-5), which has a grid diversion in the vertical direction and has a width of one cell, is expected to give a good

representation of the flow patterns observed in the flume measurements. It should however be noted that the local accelerations and decelerations within the patch are not simulated.
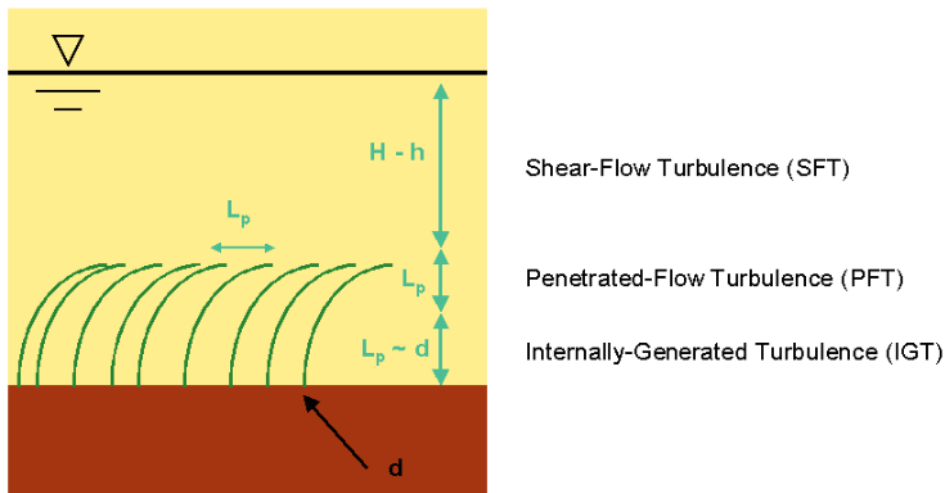
Figure 4-2 – Relevant length scales for turbulence above and in between epibenthic structures. Note that, although non-rigid structures are indicated, in this thesis the tube building worms are modelled as rigid structures (Uittenbogaard, 2003).
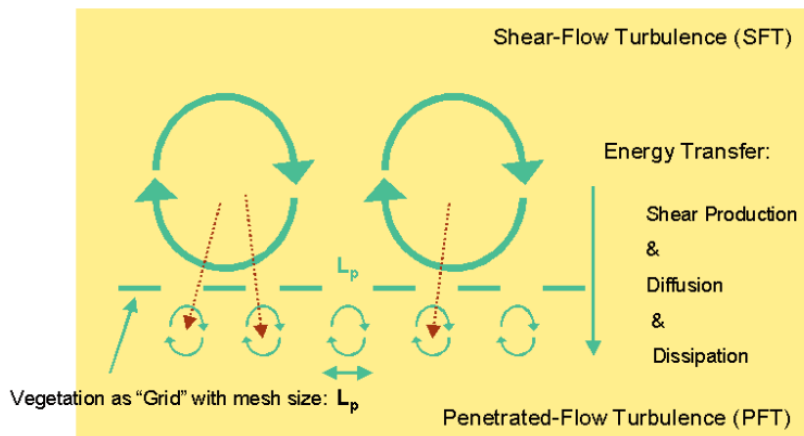
Figure 4-3 – The length scales of shear-flow turbulence reduce when the flow penetrates the worm field (Uittenbogaard, 2003).

4.3.2.2 Grid

In order to compare (and calibrate) the model results with the flume measurements, the model set-up is chosen is such a way the location of the velocity-component of model corresponds with the location of the measurements. Furthermore, the grid should be not too fine in order to reduce the calculation time of the model. However, if the grid is too coarse, the variation between calculated values of the grid cells could be too large, which could result in very non-realistic results.

Since there are no variations in the vertical velocity profiles in the y-direction, the width of the cell is set on the default setting of 1m. In the flow direction of the flume (i.e. the x-direction) the working section is simulated as 49.8 m long straight section, with the patch located in the middle of this section (Figure 4-4). Note that the length of the section in the model is larger than

the length of the flume. The long part upstream of the patch allows the variations on the velocity patterns (as result of the patch) to propagate, without being influenced by the upstream boundary condition. This also counts for the long downstream part of the patch.

Table 4-1 – Structure of the horizontal grid, which divided into five parts corresponding to the parts mentioned in Figure 4-4.

	Part I		Part II		Part III		Patch		Part IV		Part V		Part VI	
	Begin	End	Begin	End	Begin	End	Begin	End	Begin	End	Begin	End	Begin	End
Cell	1	16	17	55	56	69	70	85	86	106	107	143	144	159
x (m)	0.00	9.60	9.60	21.70	21.0	23.85	23.85	26.25	26.25	29.40	29.40	40.80	40.80	49.80
Cell size (m)	0.60		0.60-0.15		0.15		0.15		0.15		0.15-0.60		0.60	

Figure 4-4 – The horizontal grid with indicated the flow direction (from South to North), parts I-VI and the patch. Furthermore, the open boundary conditions are indicated in green, e.g. South: U=0.2 m/s; North: H=0.4m.
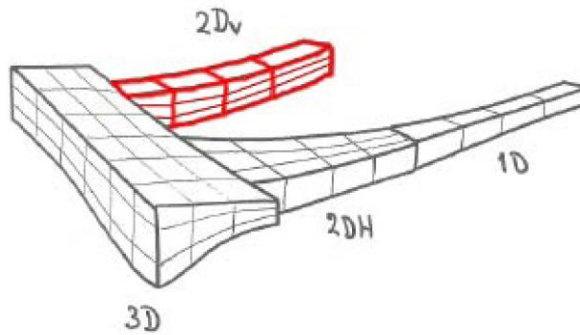
Figure 4-5 – Different ways of simulating realistic problems by varying the number of dimensions in which the model is ran. The 2DV model (bounded by red lines) is used in this report (Hoogduin et al., 2009).

In the x-direction the most variation in the velocity patterns emerges where the patch is located. These strong variations require a fine grid. In order to limit the calculation-time of the model, the grid cells from 3 m upstream of the patch till 3 m downstream of the patch have a thickness Δx of 0.15 m (Patch - Table 4-1). The grid cells totally upstream (Part I - Table 4-1) and totally downstream (Part IV) of the working section require a less fine grid with a thickness Δx of 0.60 m. The grid cells of the part between Part I and Patch (i.e. Part II) has a gradual transition from 0.60 m to 0.15 m. The same holds for the grid cells between Patch and Part IV (i.e. Part III), but then vice versa. The exact specifications of the horizontal grid can be found in Appendix 1 Table 13-2.

The vertical grid is very fine at the bottom up to 0.10 m above the bed, since the most variation in the velocity patterns is the result of interaction of the water with the rough bed and the patch (see Appendix 1 - Table 13-1). In the top layer little or no variation in the velocity profiles, hence the thickness of the top layers is a lot larger and increases up to 10% of the total water depth.

4.3.2.3 Open boundaries

Along closed boundaries, the velocity component perpendicular to the closed boundary is set to zero (a free-slip condition). At the open boundaries, the two following types of boundary

conditions are specified: water level and velocity (in the direction perpendicular to the boundary). The upstream boundary condition, i.e. the South boundary condition, is specified by the velocity (0.1 or 0.2 ms^{-1}) of the experiment setting that has to simulated (Figure 4-4). The downstream boundary condition, i.e. the North boundary condition, is specified by the water level (0.40 m) of the experiments. Both the boundary conditions are fixed during the whole simulation. As these boundary conditions are specified in time, these conditions serve as initial conditions in order to solve the continuity, momentum, turbulence and dissipation equations.

Additionally, in the case of 3D models, the use of either a uniform or logarithmic velocity profile at inflow boundaries has to be prescribed. In this report a logarithmic velocity profile is chosen, since for natural system (like the North Sea) the flow can be characterized as hydraulically rough.

5 Sensitivity analysis

5.1 Introduction

The construction of a good model consists of the following parts: the model set up, sensitivity analysis, calibration and validation (De Jong, 2005). The model set up, which has been described in the previous chapter, gives a model based on hydrodynamics and sediment transport with an essential enclosure for rigid epibenthic structures like the tube building worm, *Lanice conchilega*.

In order to investigate the behaviour of a water flow through and over a patch of tube building worms in a flume, it is necessary to determine the sensitivity of internal properties of such a flume first. For a complete overview, in this chapter both model variables and parameters will be analysed. There is a clear difference between variables and parameters. A variable represents a model state and may change during the simulations, while a parameter commonly is used to describe objects statically. In this thesis, the model parameters are constants during the complete simulation, and are not changed for varying the model variables.

First, the effects of two variables on the hydrodynamics and sediment transport will be analysed. Important variables of influence at the flow through and over epibenthic structures are: the patch density, patch height, cylindrical diameter (worm diameter), water level, flow velocity and drag coefficient. In this research, the mean focus is on the patch density and the flow velocity.

Second, after analysing the model variables, the model variables are analysed. Now, the sequence of parameters for the calibration can be determined. Like focussing binoculars, the sequence of varying the calibration parameters begins with the most sensitive parameter and ends with the least sensitive parameter.

In this chapter, the first paragraph describes the method for the sensitivity analysis. In the second paragraph the results of this sensitivity analysis are given and interpreted. Last, this is followed by conclusion of these results. The graphs referred to in this chapter can be found in 39 and are labelled with same names as the corresponding sections.

5.2 Method

First, for a complete overview, the influence of two variables on the hydro- and sediment dynamics will be analysed. These influences are obtained by varying the variables, the patch density of the tube building worm fields and the flow velocity. The patch density is varied for three different patch densities (1632, 2448 and 3264 individuals/m^2) and the stream velocity is varied for two different velocities (0.1 and 0.2 m/s). Both the patch densities and the stream velocities are chosen such that they correspond with the values used for the flume measurement and that they are realistic values for a typical North Sea environment.

The influences of different patch densities and stream velocities are derived from the velocity, turbulent kinetic energy, turbulent kinetic energy dissipation and maximum bed shear stress profiles over the whole cross section. By analysing the results over the whole cross section there

will be a complete impression of what the influences of different patch densities and stream velocities are.

After the study to the influences of the two different variables on the hydrodynamics and sediment transport, there will be an extensive examination on the influences of different parameters. Four different parameters are examined for their influences: the bed roughness, the vertical background viscosity, the horizontal background viscosity and last the effective height. The reason the parameter 'effective height' has been used as a calibration parameter, was because the measurement data did not followed the expected and common logarithmic velocity profile (see for a more extensive description Chapter 6).

The sensitivity of the four parameters is tested by varying the parameters for a low, medium and high value. The influences are derived for the velocity profile on three different positions along the cross section of the model grid (30, 15 and 0 cm before the patch of tube building worms). Like the specific values for the patch density and flow velocity, the values for these positions correspond with those used for the flume measurements. However the variables are varied for the calibration, in the sensitivity analysis for the four parameters specific values for the patch density and flow velocity, which represent a realistic North Sea environment (2448 individuals/m^2 and 0.2m/s respectively), were used. This delivers a fast interpretation of the influences of the parameters on the hydro- and sediment dynamics. Because the influence of the parameters is more or less for different variables, only one set of values for the variables is necessary.

Like focussing binoculars, the sequence of varying the model parameters begins with the most sensitive parameter and ends with the least sensitive parameter. Four important model parameters will be analysed before the calibration can be started. First, the bed roughness will be evaluated followed by the eddy background viscosity (horizontal and vertical).

The physical parameters used for the sensitivity analysis can be found in Table 5-1. The remaining model parameters, for which no input values could be determined from flume measurement data, will be varied for typical North Sea situations (Table 5-1, labelled with *). The influence of the parameters will be evaluated for smaller values (80%), greater values (120%) and the value itself. Finally, the effective height i.e. the water depth will be evaluated.

Table 5-1 – Physical parameters used in Delft3D for the sensitivity analysis.

Physical parameters	Value			[-]
	80%	100%	120%	
Gravity	-	9.81	-	m/s^2
Water density	-	1023	-	kg/m^3
Roughness (Chézy)*	52	65	78	m$^{1/2}$/s
Background horizontal viscosity*	80	100	120	·10^{-6} m^2/s
Background vertical viscosity*	80	100	120	·10^{-6} m^2/s
Effective height	0.32	0.40	0.48	m
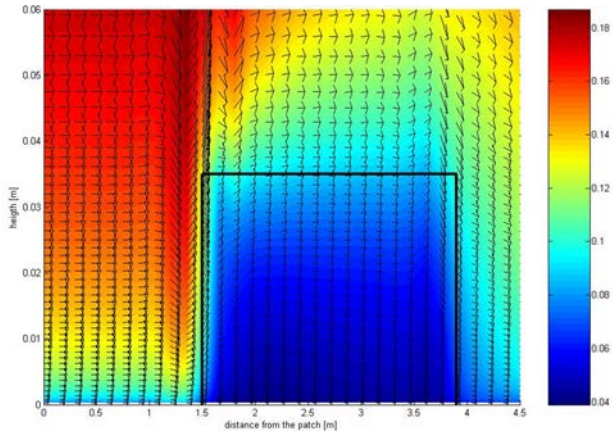
Figure 5-1 – Flow velocity in the x-z-plane with a density D of 1632 ind./m² and a flow velocity u of 0.2 m/s. The black box indicates the patch of worms.
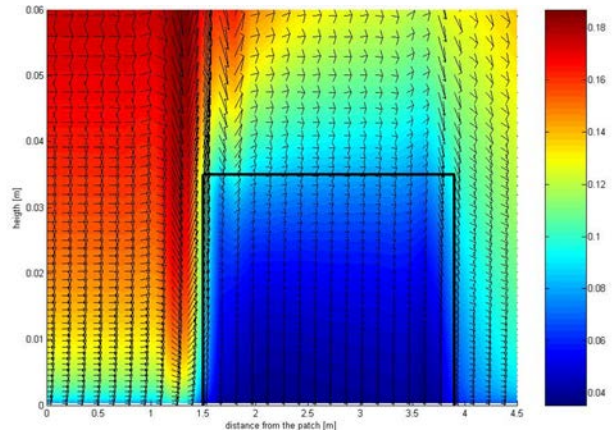
Figure 5-2 – Flow velocity in the x-z-plane with a density D of 2448 ind./m² and a flow velocity u of 0.2 m/s. The black box indicates the patch of worms.
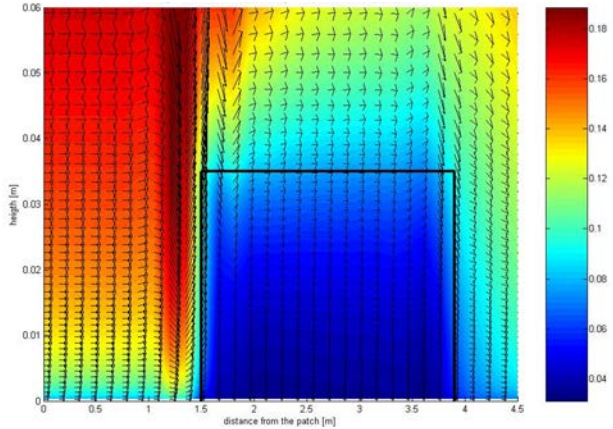
Figure 5-3 – Flow velocity (m/s) in the x-z-plane with a density D of 3264 ind./m² and a flow velocity u of 0.2 m/s. The black box indicates the patch of worms.
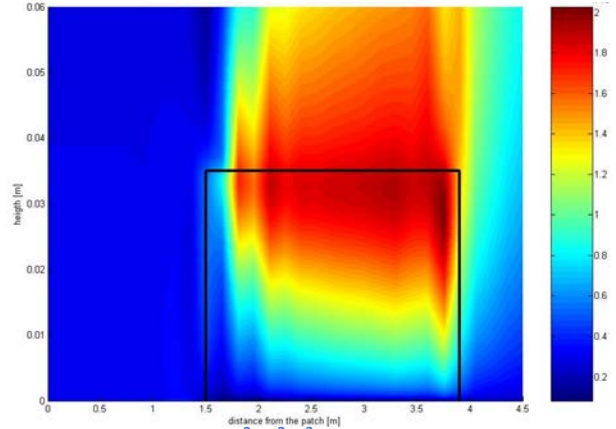
Figure 5-4 – Turbulence (·10⁻³ m²/s²) in the x-z-plane with a density D of 1632 ind./m² and a flow velocity u of 0.2 m/s. The black box indicates the patch of worms.
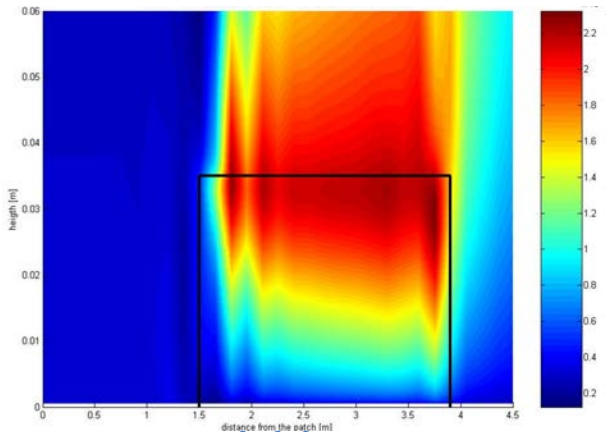
Figure 5-5 – Turbulence (·10⁻³ m²/s²) in the x-z-plane with a density D of 2448 ind./m² and a flow velocity u of 0.2 m/s. The black box indicates the patch of worms.
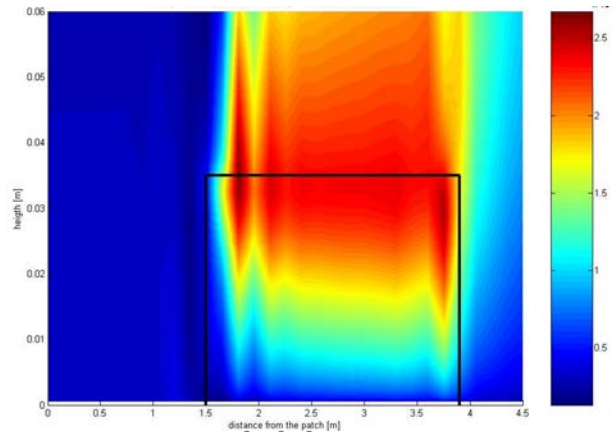
Figure 5-6 – Turbulence (·10⁻³ m²/s²) in the x-z-plane with a density D of 3264 ind./m² and a flow velocity u of 0.2 m/s. The black box indicates the patch of worms.

5.3 Results

5.3.1 Field variables

5.3.1.1 Effect of patch density

The patch density has a great influence on the flow profiles and thereby on the sediment dynamics. The friction force by the tube building worms is increased by an increasing patch density, resulting in (1) a greater deceleration within the patch; (2) a greater acceleration above the patch; (3) a stronger uplift in front of the patch and (4) a greater acceleration in front of the patch (Figure 5-1-Figure 5-3).

From Figure 5-4-Figure 5-6 becomes clear that for the turbulent kinetic energy profiles the maximum of the generated turbulent kinetic energy is at the leading edge of the patch. Here, at the tips of the tube building worms, the most turbulent kinetic energy is generated as the flow hits the tube building worms with the highest velocity. Consequently, the generated turbulent kinetic energy increases for higher patch densities. The biggest growth in the turbulent kinetic energy maxima, almost 45%, is measured for the highest patch density and flow velocity.

Besides the increase of the turbulent energy for an increasing patch density, there is also a shift in the location of the maximum turbulent kinetic energy. For higher densities, the area of the wake production (and thereby the maximum level in turbulent kinetic energy) slightly moves upstream to the front of the patch and bit above the patch. This indicates the so-called skimming flow. Here, there is the situation in which objects protruding from the bed and hinder the flow to such a degree that the main body of water passes over them instead of through them, thereby preventing sediment from the bed to erode (Eckman et al., 1981). Furthermore, there is also noticed an increase in the area of wake production for an increasing patch density.

The turbulent kinetic energy that has built up at the leading edge of the patch is dissipated downstairs along the tube building worms. The large eddies above the patch are converted in smaller eddies, when they penetrate into the patch and thereby create more enstrophy. The turbulent motions creating stronger viscous stresses and, finally, dissipate more energy.

Consequently, for increasing levels of turbulent kinetic energy by an increasing patch density, the dissipation levels increases. In the Figure 5-9-Figure 5-11 this becomes clear. Similar to the distribution of the TKE, the energy dissipation within the patch declines and is distributed more above the patch into the water flow.

The influences of the patch density on the sedimentation processes are given by the variation in bed shear stress. The bed shear stress increases for an increasing velocity gradient, which results in more erosion. The highest velocity gradients are noticed before the patch. Here, the flow encounters an uplift and accelerates. The bed shear stress increases for an increasing patch density (Figure 5-7). Similar to this erosion process, the effect of sedimentation could be noticed within the patch, where the velocity gradients, and so the bed shear stresses are very small.

This effect of velocity gradients on the bed shear stress are shown at Figure 5-8. Here the bed shear stress follows the velocity gradient: in the front of the patch there will be more erosion due higher velocity gradient due higher patch densities. Within the higher density patches the flow gradients are lower, resulting in lower bed shear stresses and, thus, more sedimentation.
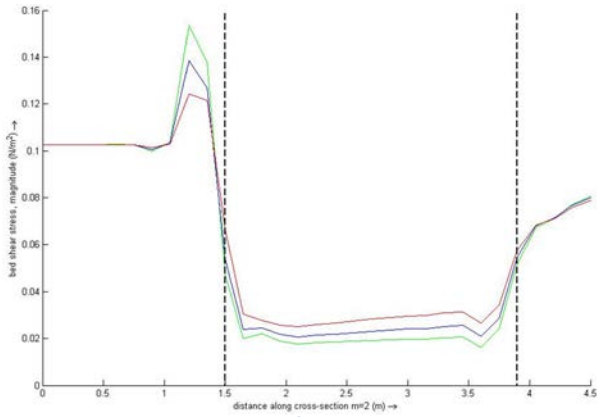
Figure 5-7 – Bed shear stress (N/m^2) in the x-direction with a density D of 1632, 2448, 3264 ind./m^2 (red, blue and green line, respectively) and a flow velocity u of 0.2 m/s. The dashed lines indicate the patch of worms.
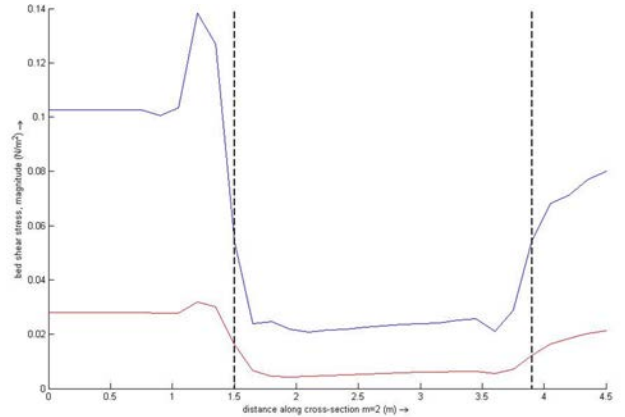
Figure 5-8 – Bed shear stress (N/m^2) in the x-direction with a density D of 2448 ind./m^2 and a flow velocity u of 0.1 and 0.2 m/s (red and blue line, respectively). The dashed lines indicate the patch of worms.
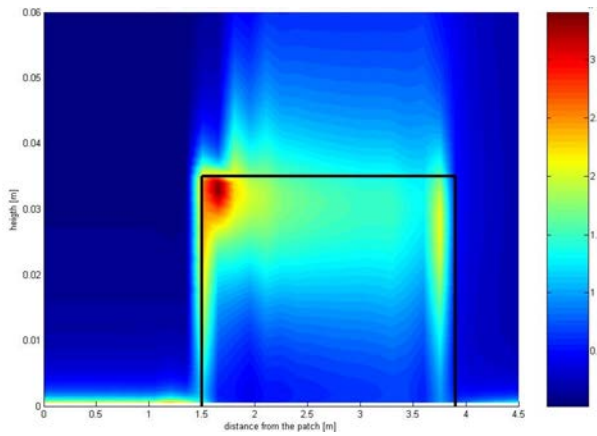
Figure 5-9 – Dissipation ($\cdot 10^{-3}$ m^2/s^3) in the x-z-plane with a density D of 1632 ind./m^2 and a flow velocity u of 0.2 m/s. The black box indicates the patch of worms.
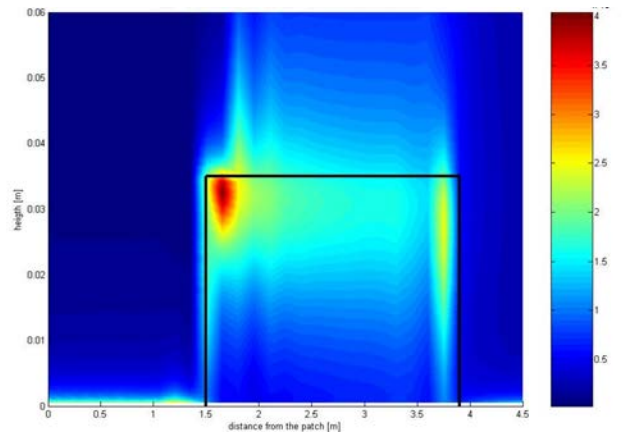
Figure 5-10 – Dissipation ($\cdot 10^{-3}$ m^2/s^3) in the x-z-plane with a density D of 2448 ind./m^2 and a flow velocity u of 0.2 m/s. The black box indicates the patch of worms.
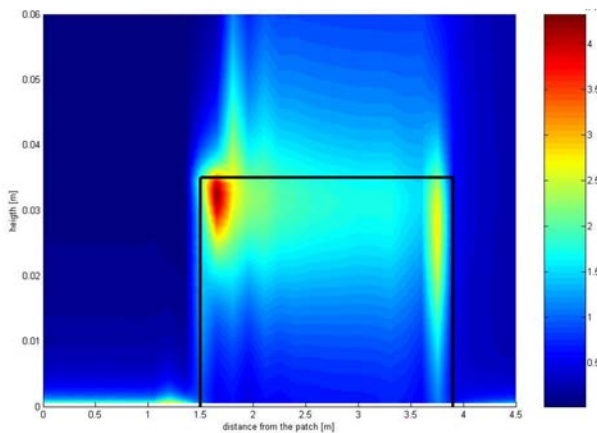
Figure 5-11 – Dissipation ($\cdot 10^{-3}$ m^2/s^3) in the x-z-plane with a density D of 3264 ind./m^2 and a flow velocity u of 0.2 m/s. The black box indicates the patch of worms.

5.3.1.2 Effect of flow velocity

Both the patch density and the stream velocity have a significant effect on the hydrodynamics and on the sediment dynamics. The highest velocity gradients are found at the tips of the leading edge of the patch, where the water hits the patch with the highest velocity (Figure 5-12 - Figure 5-13). Consequently, for an increasing flow velocity the production of TKE increases (Figure 5-14-Figure 5-15). This great enlargement in levels of turbulent kinetic energy could reach levels of almost twenty times the level at the smallest patch density. Like for an increasing patch density, there is a horizontal movement of the maximum TKE level to the leading edge of the patch.

Besides the increase in turbulent kinetic energy, there is also an increase in the area of wake production at an increasing stream velocity. Furthermore, like for increasing the patch density, also for increasing stream velocities there slightly is a horizontal movement of the highest turbulent kinetic energy level to the front of the patch. This indicates on skimming flow conditions (Friedrichs et al., 2000).

The levels of the energy dissipation at the front of the patch could rise with more than eighty times for an increasing flow velocity (Figure 5-16 - Figure 5-17). Compared to the back of the patch, the energy dissipation could raise with almost a factor 60. Instead for a change patch density, there is no significant movement in the maxima in levels of energy dissipation.

5.3.2 Model parameters

5.3.2.1 Roughness

When varying the roughness coefficient (Chézy coefficient) the velocity profiles changes a lot. For a declining Chézy coefficient i.e. for a rougher bed the flow velocity near the bed (the first 3 cm) declines. So for the part near the bed the slope of the velocity profiles increases for a declining Chézy coefficient (Figure 5-18). Above the 3 cm into the water flow, the slope flow velocity profiles gets lower and will be exceeded by slope for the 'normal' Chézy coefficient. This is to compensate the 'velocity losses' near the bed i.e. to get the same average velocity for the total height.

Following the previous interpretations for an increasing Chézy coefficient, the velocity near the bed will increase because of the less rough bed. The slope for the velocity profiles for a higher Chézy coefficient will be lower near bed and above 3 cm higher (Figure 5-18).

5.3.2.2 Background eddy viscosity

Vertical

By increasing the vertical background eddy viscosity the flow gets more viscous. The 'normal' logarithmic velocity profile is damped by the background eddies. As result of a greater background viscosity the eddies have a greater length scale and so there is a better momentum transfer of the flow. By this momentum transfer there is more even distributed velocity in the flow. Figure 5-19 shows that for a higher vertical background eddy viscosity the velocity profile is less logarithmic i.e. more even distributed. Also, positive flow velocities in the flow direction (u) are noticed. This indicates on higher shear stresses at the bed as result of the increased vertical background eddy viscosity.
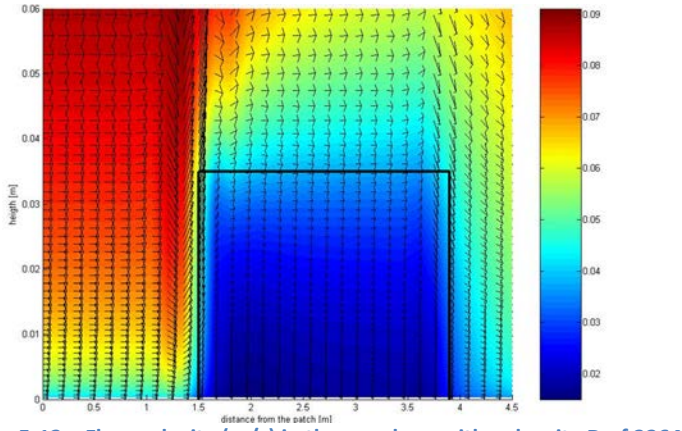
Figure 5-12 – Flow velocity (m/s) in the x-z-plane with a density D of 3264 ind./m² and a flow velocity u of 0.1 m/s. The black box indicates the patch of worms.
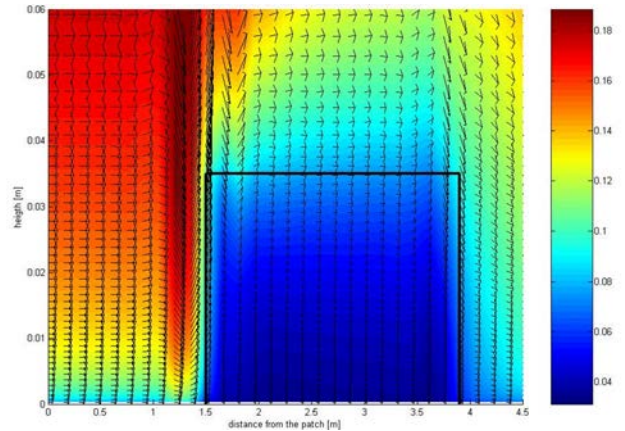
Figure 5-13 – Flow velocity (m/s) in the x-z-plane with a density D of 3264 ind./m² and a flow velocity u of 0.2 m/s. The black box indicates the patch of worms.
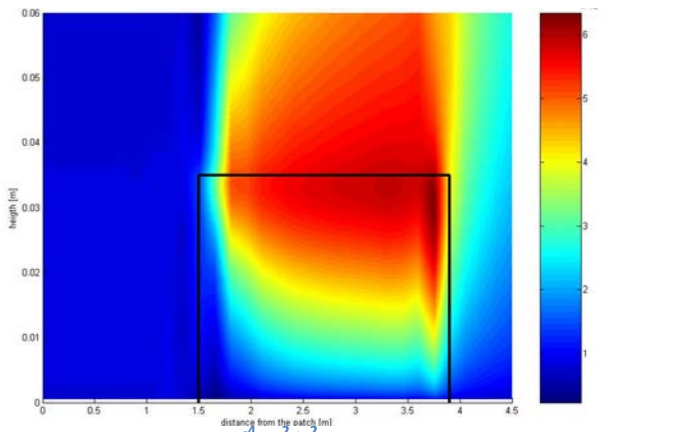
Figure 5-14 – Turbulence (·10⁻⁴ m²/s²) in the x-z-plane with a density D of 3264 ind./m² and a flow velocity u of 0.1 m/s. The black box indicates the patch of worms.
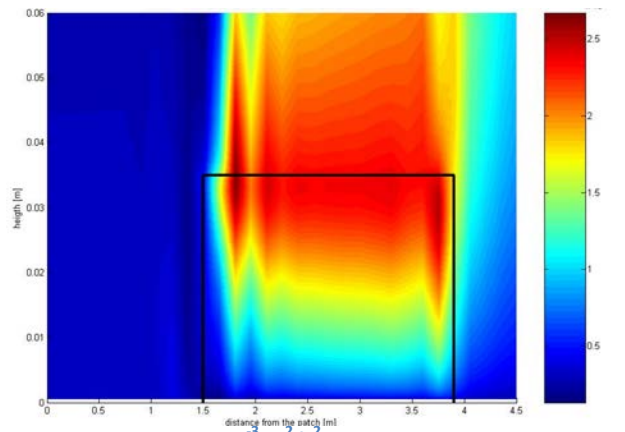
Figure 5-15 – Turbulence (·10⁻³ m²/s²) in the x-z-plane with a density D of 3264 ind./m² and a flow velocity u of 0.2 m/s. The black box indicates the patch of worms.
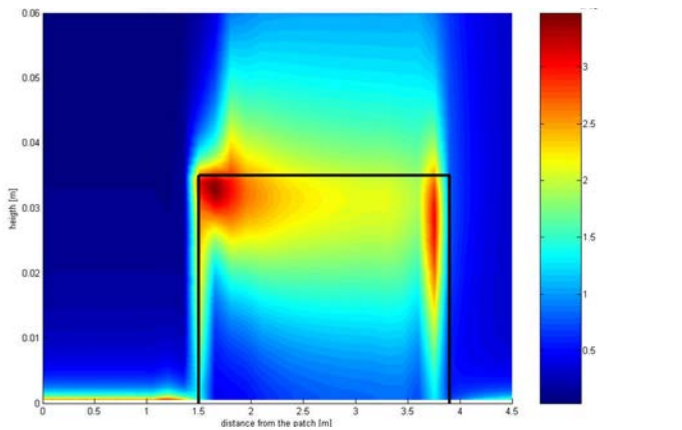
Figure 5-16 – Dissipation (·10⁻⁴ m²/s³) in the x-z-plane with a density D of 3264 ind./m² and a flow velocity u of 0.1 m/s. The black box indicates the patch of worms.
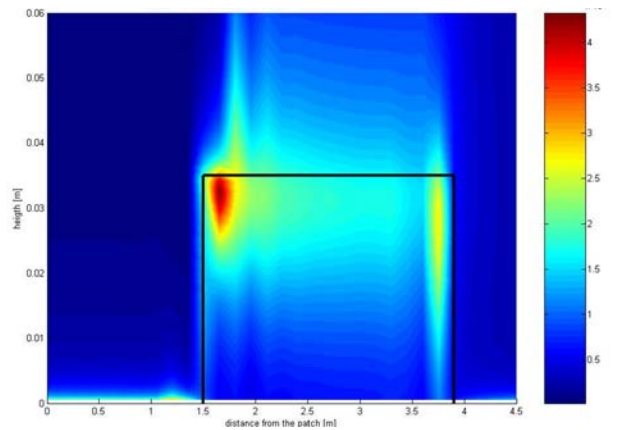
Figure 5-17 – Dissipation (·10⁻³ m²/s³) in the x-z-plane with a density D of 3264 ind./m² and a flow velocity u of 0.2 m/s. The black box indicates the patch of worms.
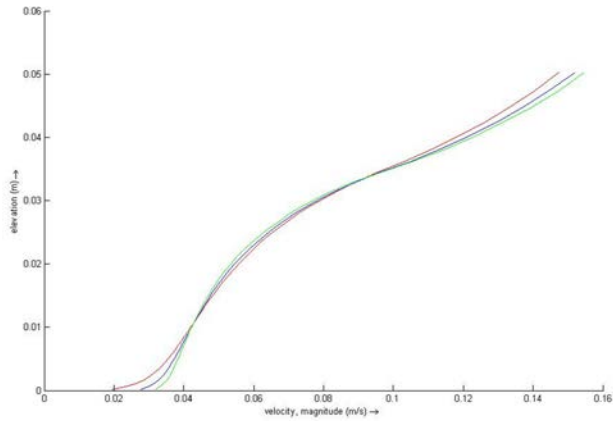
Figure 5-18 – Vertical velocity profile within the patch with a density D of 2448 ind./m^2, a flow velocity u of 0.2 m/s and a Chézy coefficient of 52, 65 and 78 m$^{1/2}$/s (red, blue and green line, respectively).
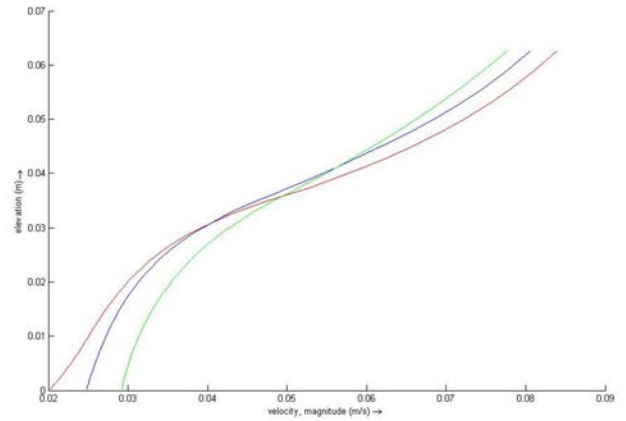
Figure 5-19 – Vertical velocity profile within the patch with a density D of 2448 ind./m^2, a flow velocity u of 0.2 m/s and a background vertical eddy viscosity of 80, 100 and 120 .10^{-6} m^2/s (red, blue and green line, respectively).
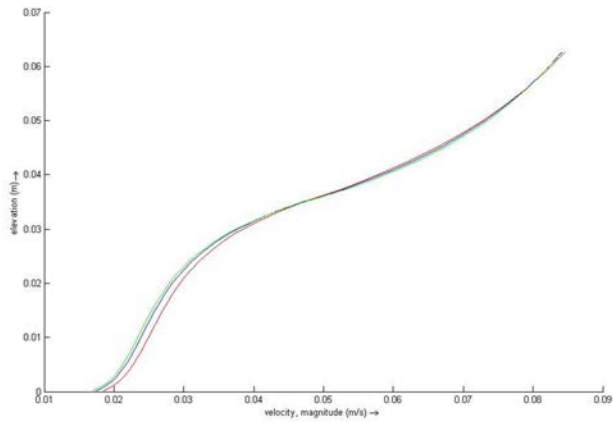
Figure 5-20 – Vertical velocity profile within the patch with a density D of 2448 ind./m^2, a flow velocity u of 0.2 m/s and a background horizontal eddy viscosity of 80, 100 and 120 .10^{-6} m^2/s (red, blue and green line, respectively).
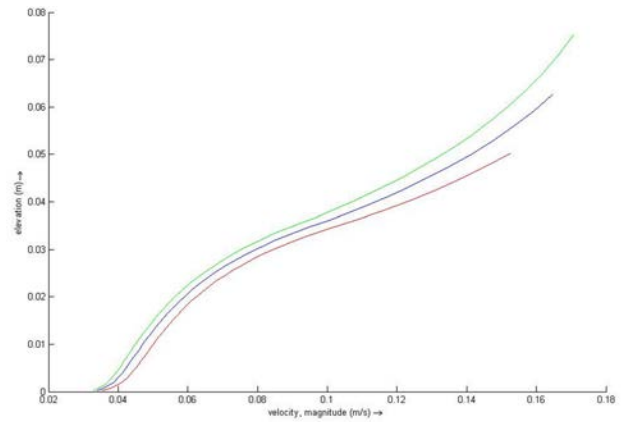
Figure 5-21 – Vertical velocity profile within the patch with a density D of 2448 ind./m^2, a flow velocity u of 0.2 m/s and an effective height of 0.32, 0.40, 0.48 m (red, blue and green line, respectively).

Horizontal

By adjusting the horizontal background eddy viscosity the velocity profile experiences the same transformation as by adjusting the Chézy coefficient. Like an increasing Chézy coefficient, an increasing horizontal background eddy viscosity allows the flow near the bed to be more developed (Figure 5-20). Actually, the momentum of the flow is better transferred for an increasing horizontal background eddy viscosity, what results in a more even distributed velocity profile. Accordingly to the previous interpretations, the velocity profile will develop slower for a declining horizontal background eddy viscosity.

5.3.2.3 Effective height

The reason for introducing the 'effective height' is to compensate the discrepancy in the velocity profile as result of the not well into motion brought water column by the conveyor belt system. For a smaller effective height the slope of the velocity profile is a lot smaller (Figure 5-21). So, the water flow is developed a lot faster for a smaller effective height.

5.4 Summary

The sensitivity analysis executed in this chapter showed that a water flow is very sensitive to variations of numerical properties. Varying the variables led to a better insight about the behaviour of the water flow through and over the patch. By varying the model parameters the sequence of calibration – beginning with the most sensitive parameter – can be determined. Table 5-2 presents the analysed variables and parameters with their particular influence on the flow.

Table 5-2 – Results of sensitivity analysis: ++ Strong significant influence, + significant influence, +/- minor influence, - insignificant influence.

Variables	Velocity profile	Turbulent kinetic energy	Energy dissipation	Bed shear stress
Patch density	++	+	+/-	++
Flow velocity	++	++	++	++
Parameters				
Roughness coefficient	++			
Vertical background eddy viscosity	+			
Horizontal background eddy viscosity	+			
Effective height	++			

6 Calibration

6.1 Introduction

The construction of a good model consists of the following parts: the model set up, sensitivity analysis, calibration and validation (De Jong, 2005). The model set up and sensitivity analysis have been done in the previous two chapters. The calibration that will be described in this chapter includes the comparison of the mathematical model, Delft3D, with the measurement data from the flume, and the adjustment of its underlying assumptions or equations to achieve a better fit with the reality. In this thesis the part of adjustment of underlying assumptions or equations is satisfied by varying some characteristic parameters. Afterwards there will be an analysis of the residual errors.

The validation is the process of determining the degree to which the calibrated model is an accurate representation of the real world (De Jong, 2005). Here, the model output will be compared with an independent set of measurement data in order to determine whether the model reproduces the data with the required accuracy.

After the calibration and validation their significance becomes clear when there could be simulations and studies on many scenarios. However the validation could not be executed because of the lack of enough flume measurement data, there will be an implementation of the calibrated model on some typical North Sea situations in the next chapter.

In this chapter, the first paragraph describes the method for the calibration. In the second paragraph the results of this calibration are given and interpreted. Last, this is followed by discussion and conclusion of these results.

6.2 Method

The model output was calibrated against the collected flume measurement data. As described in previous chapters, the flume environment was kept the same during the whole experiment, while changing the stream velocity and the density of the tube building worms. The input model, with its grid, initial conditions and boundaries are described in Chapter 4 (Model set up). The physical parameters can be found in Table 6-1. The remaining model parameters, for which no input values could be determined from flume measurement data, were used for model calibration (see Table 6-1 labelled with *).

As discussed in the previous chapter, the roughness parameter (Chézy coefficient) and the background viscosity (horizontal and vertical) have significant influence on the velocity profiles. The influence of the background vertical viscosity on the velocity profiles becomes especially clear near bottom. There was noticed a positive displacement in the near bottom velocities for greater values of the background vertical viscosity. Greater values of the background vertical viscosity are also responsible for a less exponential velocity profile. Instead of the main influence of the background vertical viscosity on the near bottom regions, the Chézy coefficient has a great influence on both the near bottom regions as the more upper regions of the velocity profiles. The background horizontal viscosity has the slightest influence on the velocity profiles.

Afterwards, it became clear the model strongly underestimated the velocity profiles of the measurement data for larger velocities (at larges heights). Looked at the velocity profiles for the whole depth it became clear that the measurement data did not followed the expected and common logarithmic velocity profile. The reason for this discrepancy might be the conveyor belt system of the flume, which seems to create a range of heights of water that is not brought into movement properly. Following this interpretation, this influence of the conveyor belt system should increase for larger velocities. To correct this discrepancy, that the measurement data did not followed the expected and common logarithmic velocity profile for a specific height, there should be a variable that denotes on the 'effective height'. Therefore, the new calibration parameter the 'effective height' was introduced.

As described above, the calibration starts with the adjustment of the shape of the velocity profiles. Next the effective height is adjusted so the simulated velocity profiles will match with the measurement data. Like focussing binoculars, the sequence of varying the calibration parameters begins with the most sensitive parameter and ends with the least sensitive parameter. Following the results from the previous chapter, the calibration begins with varying the Chézy coefficient, followed by the background vertical viscosity and the background horizontal viscosity till the shape of the simulated velocity profile matches that of the measurement data. At the end the so-called effective height it adjusted so that velocity profiles of the simulation and the flume measurements overlay.

The velocity profiles in the patch of tube building worms have been analysed and evaluated by Friedrichs et al. (2000). The interesting part is the part before the patch of tube building worms. The behaviour of the stream in this part has still to be analysed on both a qualitative and quantitative way. The qualitative study and analyse have already been described comprehensively in Chapter 5. In this chapter the quantitative study will be described and evaluated. The grid used by the simulation has been described in the Paragraph 4.3.2 Model set-up. This grid has been chosen such that values in the grid cells are written on specific distances from the leading edge of the patch. In this way, the distances from the leading edge of the patch, derived from the means of two grid cells, matches with the distances of the measurement data.

Instead the final simulation values are derived by averaging two values, the final values for the measurement data are derived by taking the mean of three values. These three values have been derived from three different places: 5 cm before, exactly on and 5 cm behind the specific place. With averaging three values in such a manner, some points are created that behave like grid cells and have information (values for the velocity) of a range of points (like what happens in a cell), instead of just the information of one specific point. Due the very abrupt fluctuations in the stream which happen on a small scale, there could be large velocity differences between the simulation and the measured values. Therefore, averaging the measured values over a range of distances gives more reliable information for the velocity profiles.

6.3 Results

The figures derived from the flume measurements and the Delft3D simulation can be found below, Figure 6-1-Figure 6-6. The derived calibration parameters are presented in Table 6-2. Figure 6-1-Figure 6-3 show the results for the low stream velocity (0.1m/s) and those are followed by the high stream velocity (0.2 m/s) (Figure 6-4-Figure 6-6).

Table 6-1 – Physical parameters used in Delft3D for the calibration.

Physical parameters	Value	[-]
Gravity	9.81	m/s^2
Water density	1023	kg/m^3
Roughness*	55:1:80	$m^{1/2}/s$
Background horizontal viscosity*	1:25:1000	$10^{-5} \ m^2/s$
Background vertical viscosity*	1:25:1000	$10^{-6} \ m^2/s$
Effective height	10:5:40	$10^{-2} \ m$

For the low velocity (for all densities of tube building worm fields) there is a clear difference between the velocity profiles for the simulation with that for the flume measurements. Although the shape for the two different velocity profiles is near the same, for all densities there is a clear overestimation of the actual data by the simulation. This discrepancy increases with an increasing density of the tube building worm field (Figure 6-1-Figure 6-3). Furthermore, for all densities the near bottom flow at the edge of the tube building worm field is not slowed down enough compared to the flume measurements (Figure 6-1-Figure 6-3). Also, the deceleration of the near bottom flow by the tube building worm field is set in too high.

The high velocity simulations (Figure 6-4-Figure 6-6) show totally different results. Here, instead of the overestimation for the low velocity simulations, there is for all densities of worms a slight underestimation of the flume measurements by the simulations. Despite the fact that slope is a bit too small, the simulated velocity profiles follow the measurement data quite well. Nevertheless, similar to the low velocity simulations, the deceleration of the near bottom flow by the tube building worm field is set in too high.

Table 6-2 – Physical parameters determined by the calibration in Delft3D.

Physical parameters	Value	[-]
Roughness	74	$m^{1/2}/s$
Background horizontal viscosity	2.0	$10^{-3} \ m^2/s$
Background vertical viscosity	3.0	$10^{-4} \ m^2/s$
Effective height (u=0.1 m/s)	20	$10^{-2} \ m$
Effective height (u=0.2 m/s)	40	$10^{-2} \ m$
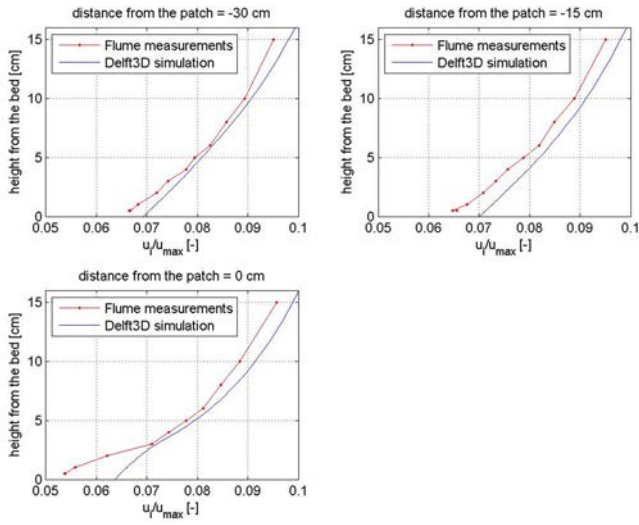
Figure 6-1 – The velocity profiles for the flume measurements (red line) and the simulation results (blue line) on different distances in front of the leading edge of the patch: 30 cm (a), 15 cm (b) and 0 cm (c); u = 0.1m/s; n = 1632 individual/m².
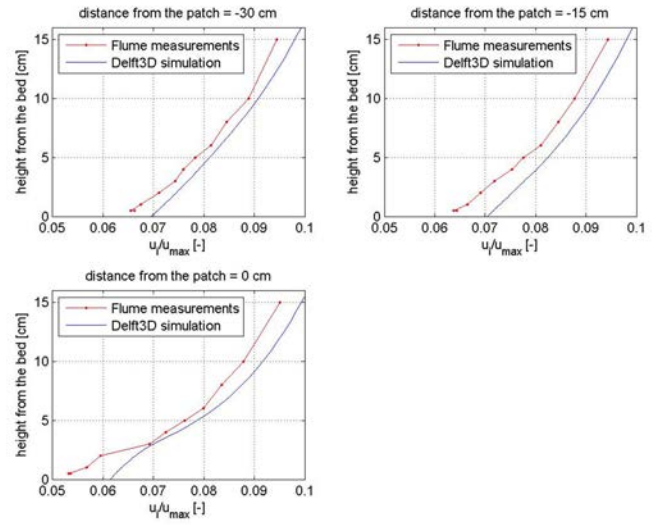
Figure 6-2 – The velocity profiles for the flume measurements (red line) and the simulation results (blue line) on different distances in front of the leading edge of the patch: 30 cm (a), 15 cm (b) and 0 cm (c); u = 0.1m/s; n = 2448 individual/m².
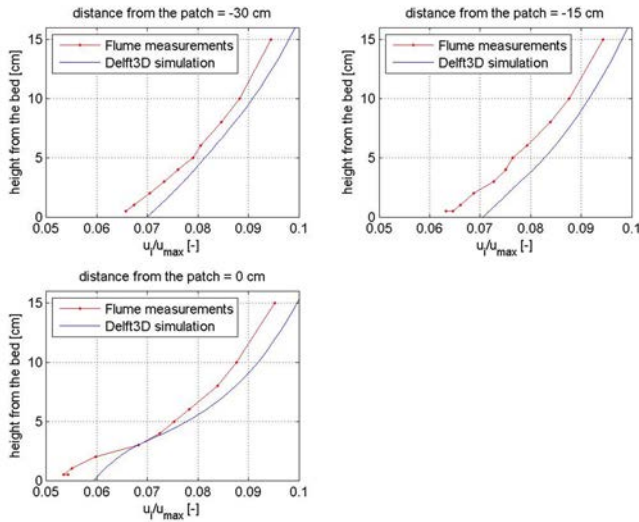
Figure 6-3 – The velocity profiles for the flume measurements (red line) and the simulation results (blue line) on different distances in front of the leading edge of the patch: 30 cm (a), 15 cm (b) and 0 cm (c); u = 0.1m/s; n = 3264 individual/m².
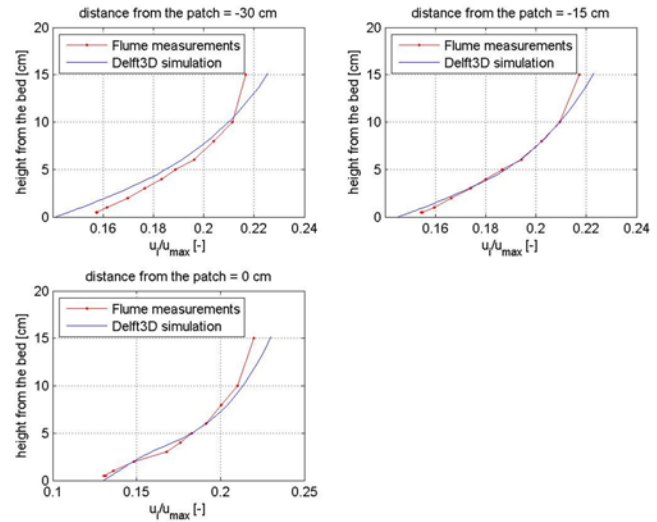
Figure 6-4 – The velocity profiles for the flume measurements (red line) and the simulation results (blue line) on different distances in front of the leading edge of the patch: 30 cm (a), 15 cm (b) and 0 cm (c); u = 0.2m/s; n = 1632 individual/m².
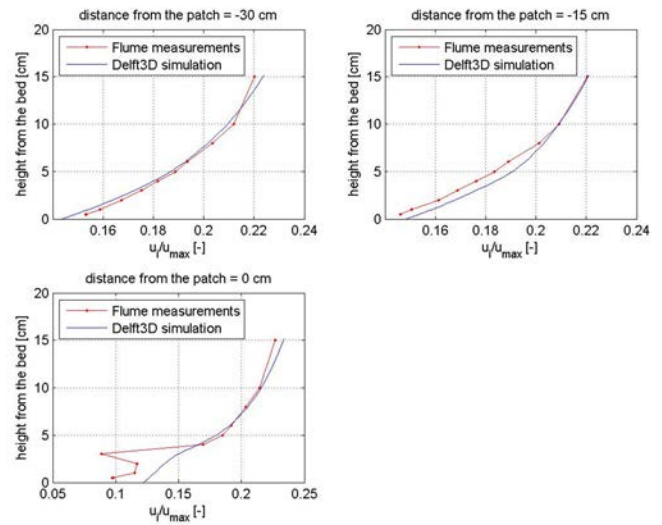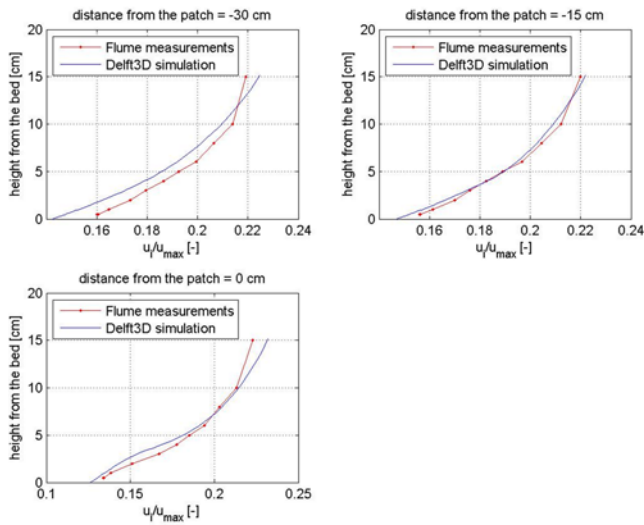
Figure 6-5 – The velocity profiles for the flume measurements (red line) and the simulation results (blue line) on different distances in front of the leading edge of the patch: 30 cm (a), 15 cm (b) and 0 cm (c); u = 0.2m/s; n = 2448 individual/m².

Figure 6-6 – The velocity profiles for the flume measurements (red line) and the simulation results (blue line) on different distances in front of the leading edge of the patch: 30 cm (a), 15 cm (b) and 0 cm (c); u = 0.2m/s; n = 3264 individual/m².

6.4 Conclusion

The calibrated model shows a much more realistic view of the velocity profiles. Although the simulations approximate the flume measurements rather accurate, there are still some deviations. The smallest deviations are for the high velocity profiles. The stream velocities in typical North Sea circumstances are the most comparable with the chosen high velocity, so the simulations give us a realistic impression of the flow near the bottom. For this reason this calibrated model could give good predictions on the bed shear stress and therefore good predictions on the sediment dynamics. Furthermore, the margin of error in the velocity profiles is realistic compared to the model discrepancies of Bouma et al. (2007).

However the calibrated model performs rather well, there should be collected more data so the calibrated model can be validated. Also, the quality of the data should be increased. In the used data there is still a discrepancy probably as result of the conveyor belt system, which creates a package of water that is not brought into movement properly.

7 Implementation

7.1 Introduction

In The Netherlands, there is a constant threat of flood by the North Sea. A well organised and maintained defence system is essential. Therefore, the shore is held in position by supplying sand on the beaches since 1979. Since 1990, when the Government adopted the policy called "Dynamic Preservation of the coast line", the complete coastline has been maintained at its position of 1990 in order to fulfil the desired safety levels. The further retreat of the coast by erosion has been minimized by sand nourishments (i.e. sand excavated from the bottom of the North Sea is added to the shore zone).

Besides, by the selection of beaches as protected sites (Natura 2000) and the addition of the Wadden Sea as an Unesco World Heritage Site (2009), the ecological aspects of sand nourishment have become important to be attentive to. Tube building worms could be very desirable in these areas, since studies have shown the biodiversity in the patches of tube building worms is very high compared to other species (Rabaut et al., 2007). However sand nourishment could damage the biota of the North Sea, biota can be used to support the goals of the sand nourishment: coastal stability, fulfil the coastal protection and enhance the recreation (De Ronde et al., 2003). The reason of this is because a lot of benthos are so-called bio-engineers, which roughly can be divided in stabilizers and destabilisers (Borsje et al., 2009). An example of stabilizers is diatoms, which increase the critical shear stress for erosion by gluing the sediment together (Riethmüller et al., 2000). An example of destabilisers is Tellina fibula, which make the sediment more prone to erosion due to digging and feeding activities (Austen et al., 1999).

Thus, tube building worms are able to influence both the sediment dynamics and hydrodynamics by several orders of magnitude. Besides, the tube building worms can act on a large spatial (tidal basin) and temporal (seasonal and inter-annual) scale (Borsje et al., 2009). However the benthos biomass per unit area in subtidal areas is much smaller than the benthos biomass in intertidal areas, studies have shown that it they can still influence the dynamics of the sediment and the water significantly (Borsje et al., 2008b).

Tube building worms can both act as stabilizers and destabilisers. For very small densities local scour is caused by the tubes. For more dense patches, the water is deflected around and over the patch instead of going through the patch, which results in a stabilized patch (Eckman et al., 1981). This stabilization of sediment by tube building worms is demonstrated by field experiments (Rabaut et al, 2008), flume studies (Friedrichs et al., 2000) and modelling results (Borsje et al., 2009).

7.2 Method

To determine the influence on the bed shear stress three variables investigated: the velocity of the water flow, the height of the water column compared to the height of the worms and the density of the tube building worm field. From these three variable five typical North Sea scenarios are created to determine the influence of these variables on the bed. The creation of typical North Sea situations depends on whether the variables have a positive or negative influence on the bed, so that no scenarios are created with contradicting effects on the bed shear stress.

The flow velocity has a positive influence on both the bed shear stress maximum before the patch (and around the patch in reality, a three-dimensional situation) and on the bed shear stress minimum in the

patch (Figure 5-8). Thus, the bed shear stress on the complete bed increases as result of an increasing flow velocity. In Figure 7-1 becomes clear that an increasing height of the water column has the opposite effect, a negative effect, on the complete bed shear stress profile. Neither this negative influence nor the positive influence on the complete bed shear stress profile, as result of an increasing water depth and an increasing flow velocity respectively, is noticeable for an increasing patch density. When increasing the patch density, the bed shear stress before the patch increases and the bed shear stress within the patch it declines. So, because of the increased flow deceleration within and the increased flow acceleration before the patch, varying the patch density has both a positive and a negative influence on the bed shear stress profile (Figure 5-7).

With this qualitative determination of the influence on the bed shear stress, five scenarios are created by the variable values from Table 7-1 which are obtain by Borsje et al. (2009), Rabaut et al. (2007), Bouma et al.(2007) and Ropert and Dauvin (2000). Of the three variables, the flow velocity is the most sensitive. Therefore, the flow velocity was the 'leading' variable for creating the five scenarios mentioned in Table 7-1. The results are coupled by their way of influencing the bed shear stress (positive or negative) according:

$$U(1 - \lambda)\frac{h_{TBW}}{\zeta} \tag{46}$$

where U is the bulk flow velocity (m/s) and h_{TBW}/ζ (-) the ratio of the worm height h_{TBW} and the water level elevation ζ. λ, the specific rod area (-), is specified by Eq. 41.
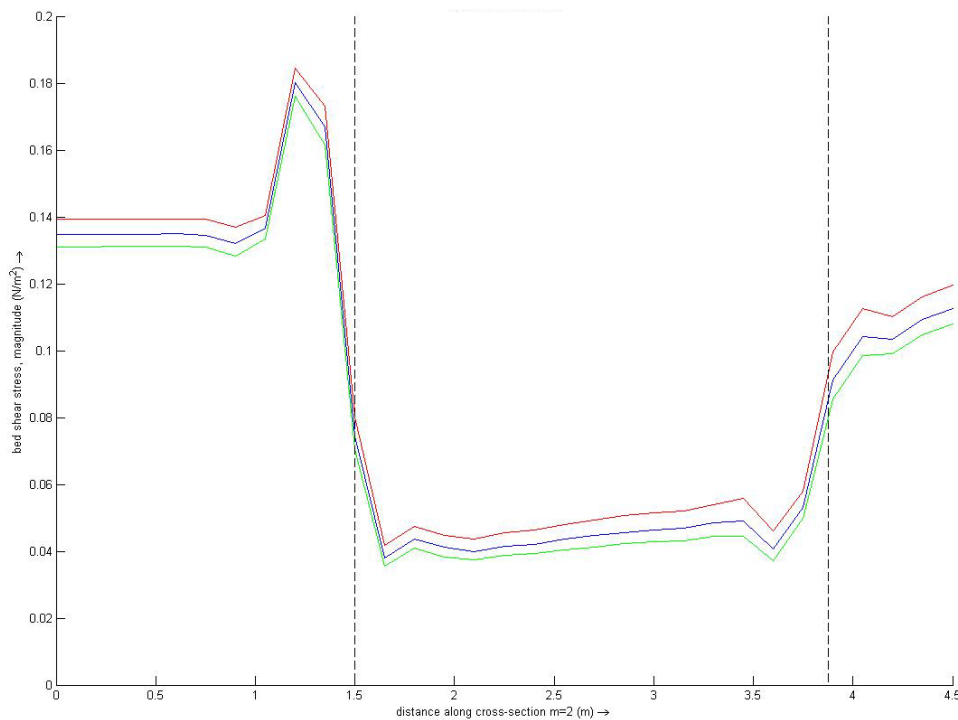
Figure 7-1 – Bed shear stress (N/m^2) in the x-direction with a density D of 2448 ind./m^2, a flow velocity u 0.2 m/s and an effective height of 0.32, 0.40, 0.48 m (red, blue and green line, respectively). The dashed lines indicate the patch of worms.

Table 7-1 – Implemented scenarios in Delft3D for determining the influence on the bed shear stress. The scenario values are obtained from Borsje et al. (2009), Rabaut et al. (2007), Bouma et al.(2007) and Ropert and Dauvin (2000).

Scenario	U [m/s]	m [ind./m^2]	λ[-]	H [m]
1	0.15	5000	0.0981	30
2	0.20	4000	0.0785	25
3	0.25	3000	0.0589	20
4	0.30	2000	0.0393	15
5	0.35	1000	0.0196	10

7.3 Results

From Figure 7-2 becomes clear that for more extreme situations (i.e. scenario 4 and 5) the bed shear stress increases rapidly. The maximum bed shear stress before the patch follows this pattern and can be even 60% higher than in the case of no patch of tube building worms. The minimum bed shear stress in the patch is much lower than in the case of no patch, indicating on the stabilizing effect of the tube building worms already at 1000 individual per unit area. Like for the maximum bed shear stress, the minimum bed shear stress in the patch increases for the more extreme scenarios as result of lower patch densities, higher flow velocities and lower bed levels.

Remarkably, the scaled maximum bed shear stress increases for the less extreme scenarios, while the minimum bed shear stress decreases (see Figure 7-3). Looking at the response of the bed shear stress, while changing the variables, this could indicate that for the less extreme scenarios the contribution of the patch density is more significant.

The small decrease in the scaled maximum bed shear stress, when going from scenario 2 to scenario 1, could be caused by a too coarse grid. The bed shear stress figures (Figure 5-7, Figure 5-8, Figure 7-1, Figure 15-1-Figure 15-3) show a slightly smaller region where the maximum bed shear stress occurs. The horizontal grid distance of 15 cm is relatively big compared to this maximum bed shear stress region (30-50 cm). So the probability of not giving the 'real' maximum bed shear stress is relatively high.

7.4 Conclusion

For more extreme situations the bed shear stress increases rapidly compared to a situation of no occurrence of tube building worms: up to 60% increase of bed shear stress levels before the patch and a decrease of bed shear stress levels within the patch of at least 80%. The pattern of the scaled bed shear stress levels behave differently. In more extreme situations the scaled bed shear stress levels decrease before the patch and increase within the patch. This could indicate on less influencing effects of the tube building worms (i.e. the density of the patch) for more extreme situation, which results in less stabilizing effects.

The small decrease in the scaled maximum bed shear stress, when going from scenario 2 to scenario 1, could be caused by a too coarse grid. Since the horizontal grid distance is relatively big compared to this maximum bed shear stress region, the probability of not giving the 'real' maximum bed shear stress is relatively high.
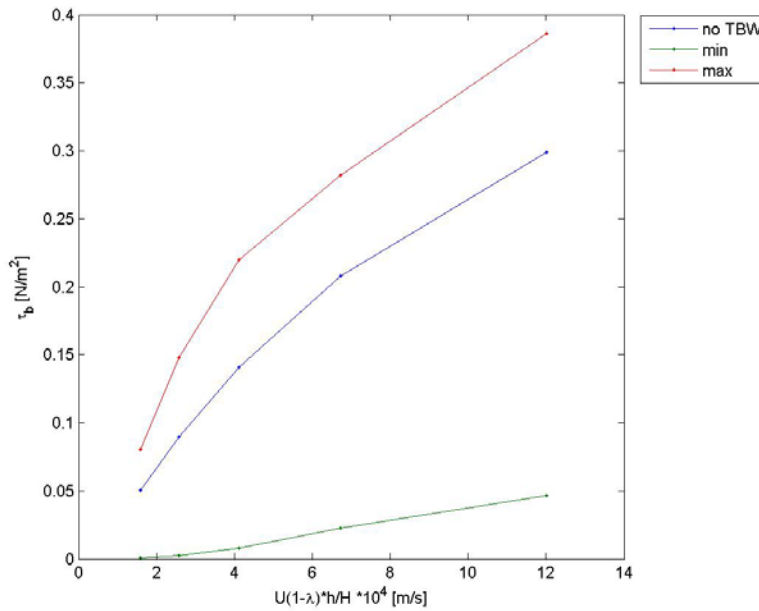
Figure 7-2 – The bed shear stress values for scenarios 1-5. The blue line represents the bed shear stress for all scenarios if there are no tube building worms. The green line represents the minimum bed shear stress (i.e. the bed shear stress within the patch) for all scenarios if there are tube building worms. The red line represents the maximum bed shear stress (i.e. the bed shear stress before the patch) for all scenarios if there are tube building worms.
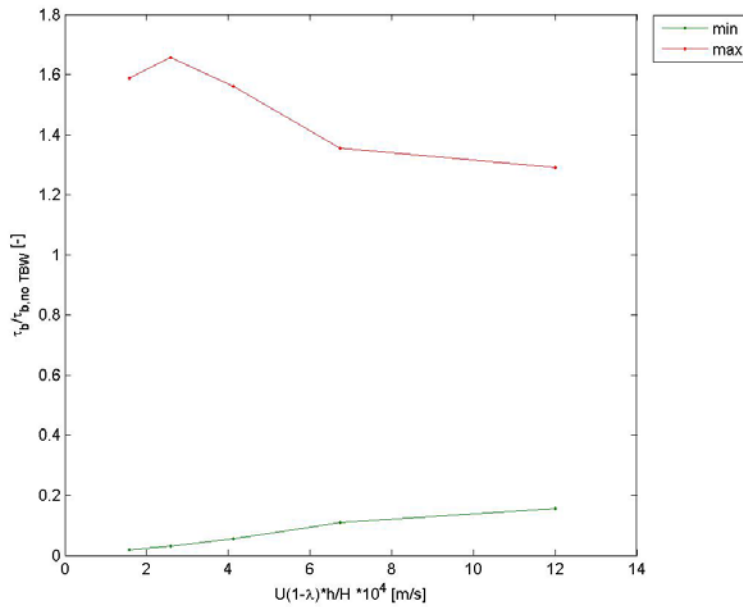
Figure 7-3 – The minimum and maximum bed shear stress values scaled with the bed shear stress if there are no tube building worms for scenarios 1-5. The green line represents the minimum scaled bed shear stress (i.e. the bed shear stress within the patch) for all scenarios if there are tube building worms. The red line represents the maximum scaled bed shear stress (i.e. the bed shear stress before the patch) for all scenarios if there are tube building worms.

8 Discussion

From the results described in the previous chapters some conclusions can be made. There are however some remarks that make these conclusion rather uncertain. Some uncertainties emerge in multiple part of this study. Therefore, in order to keep the source of the uncertainties clear, only distinction between the methodology and the results are made. Within these paragraphs, the same structure of Chapter 2 till 6 is applied on the discussion.

8.1 Discussion on methodology

In this study, recent flume data results have been modelled by a three-dimensional hydrodynamic model in order to be able to up-scale flume experiments to field conditions. The link between flume and field conditions is, however, not so straightforward. Consequently, before discussing the sources of the possible errors made in this study, the interrelationship between the flume experiment and the field conditions will be debated.

8.1.1 Flume vs. field

It should be noted that flow in flume tanks is always at best an idealized representation of flow in the field. In general, turbulence intensities in the flume are lower than in the field and the flume tank dimensions determine the largest eddy sizes (Bouma et al., 2007). Nevertheless, former work has indicated that turbulence levels found in the NIOO flume tank are very comparable to situations of steady flow in the field (Hendriks et al., 2006).

Furthermore, the tube building worms are represented in both the flume and the Delft3D model setting as thin smooth rigid piles. In the field, however, the tubes are made of small bed material particles, which are glued together by the tube building worm. This building process results in relatively less smooth and rigid tubes compared to standard piles. Consequently, in the field, the velocity profiles and the creation of turbulent kinetic energy will differ from those patterns in the flume and Delft3D model. Less smooth tubes will result in higher resistance and therefore in higher values for turbulent kinetic energy. In the latter situation, skimming flow will occur more likely. More flexible tubes, however, will cause lower resistance on the flow and a turbulence maximum closer to the bed (Dijkstra et al., 2006).

In the experimental and model setting the configuration of the patches was constructed in a very structured manner i.e. the tubes, with all the same diameter and height above the bed, were distributed spatially uniform into a rectangular shape. From former studies (e.g. Godet et al., 2008), however, it is know that the configuration of the patches varies considerably. Besides, the composition of the patches changes as the number of juveniles will differ throughout the year (Callaway, 2003 and Baptist et al., 2009). The absence of smaller and thinner juveniles, which are found in the field attached to the adults, could result in different hydrodynamic patterns (and therefore sediment patterns) on a very local scale.

Finally, it should be noted that the width of the patch includes the whole width of the flume tank. In this way, only the flow over the patch is simulated, since the flow is not able to flow around the patch. Although this is not a realistic representation of the field circumstances, it facilitates the focus on the research parameters since this assumption simplifies the model a lot.

8.1.2 Measurements

In order to test the predictive power of the model, two "identical" situations, viz. a flume tank experiment and a three-dimensional hydrodynamic model, are created. In the flume tank experiment, the processes which are not taken into consideration are minimized. Nevertheless, the influences of

these processes cannot be removed totally. First, the influence of the side walls of the flume tank on the flow patterns are not taken into account in the Delft3D model. This could cause some extra turbulence creation and additional energy dissipation at the side walls, which consequently influences the velocity patterns in the flume.

In the flume experiment, at every 5 cm along the flume the velocity components in three dimensions are determined by ADV. At the leading edge of the patch, however, the changes in the vertical velocity profiles are rather large. Thus, more measuring points (e.g. every 1 or 2 cm instead of every 5 cm) might give a more accurate transition of the vertical velocity profile along the flume. Although more information in this transition zone could provide a better understanding of the ongoing processes, this could easily increase the measurement time with a factor two.

8.1.3 Governing equations

In understanding the ongoing processes more, the hydraulic model Delft3D has been used. In this study, the k-ε equations are used to model the flow and turbulence patterns. The advantages of this approach are that the model is relatively simple to implement, it leads to stable calculations, and it converges relatively easily (Biswas and Eswaran, 2002). For these reasons, the model gives reasonable predictions for many flows.

A disadvantage of the k-ε model, however, is that the dissipation equation, which is derived by multiplying the k equation by (ε/k) and introducing simple model constants, is rather simplistic. This could results in not realistic model predictions for e.g. flows with strong separation that might occur at the downstream edge of the patch for high flow velocities and high patch densities. This problem can be solved by introducing equations instead of the simple model constants. Nonetheless, these equations could cause overparameterization, as they introduce some additional calibration closure constants. The large number of calibration parameters could create a situation where multiple parameter sets could come to the same solution. In this situation, the parameter sets are in fact useless, since it is unclear which parameter set should be used when up-scaling the flume data to field conditions.

Furthermore, the model uses equations that are based on assumptions which are possibly not valid for all conditions. First, it is assumed that the vertical accelerations can be neglected (the shallow water assumption). This reduces the vertical momentum equation reduces to the hydrostatic pressure equation, which leads to stable calculations that converge relatively easily and therefore gives reasonable predictions for many flow situations. In the leading edge in front of the patch, however, the flow is abruptly changed into the vertical direction. Deltares has provided Delft3D with a pressure correction technique for computing the non-hydrostatic pressure, which is computed similar to the method presented by Casulli (1999) and Busnelli (2001) and is employed in combination with an ADI-technique which differs slightly from the Delft3D model presented in Chapter 4 (Bijvelds, 2001).

In this study, this method has not been used, although it could be useful to investigate the influences of implementing this method. However the patch height compared to the total water column depth very small in the field, in the flume the change in bathymetry is significant. This could indicate that using the pressure correction technique could be helpful in understanding the processes.

The equations used in this study not take into account the influences of waves on the flow and turbulence patterns, only the influence of the tides. In deep water, the influence of tides on the morphology is at its maximum and decreases toward the shore (Liek, 2000). The influence of waves on the morphology is vice versa. Since the patches of tube building worms have been found in varying field

conditions (Heip et al., 1992;Künitzer et al., 1992 and Rabaut et al., 2007), the inclusion of the flow-wave interaction could provide more realistic predictions for up-scaling to field conditions. Other important factors that have to be taken into account are the Coriolis force, the wind, the flow-sediment interaction and the changing benthic variability. The latter two factors are described extensively by Borsje et al. (2009a,b), Bobertz et al. (2009), Friedrichs et al. (2009) and Friedrichs and Graf (2009).

Finally, in order to solve each differential equation used in Delft3D, it requires boundary and initial conditions. Although these conditions are valid for the "ideal situation" presented in the model, it could be a not completely correct representation of the reality i.e. the flow behaviour in the flume. Especially, for up-scaling the flume experiments to field conditions by including tube building worms in a numerical model, these condition could be hard to specify.

8.1.4 Model set-up

The grid used in this study is based on the flume data in order to give reasonably good results for the vertical velocity profiles along the flow direction. A finer grid, especially in the horizontal direction, will give more detailed information on the ongoing processes in the transition zone where the flow nears the patch. Implementation of a finer grid will probably give more realistic predictions, but it will increase the computation time a lot.

In order to reduce the computation time even more, a two-dimensional vertical (2DV) model is used. Although this 2DV model gives less detailed and less realistic results compared to the 3D model, the model outcomes are very comparable with the flume data.

8.1.5 Sensitivity analysis

In the sensitivity analysis, the influences of the following four different parameters on the flow and turbulence patterns were examined: the bed roughness coefficient, the vertical background eddy viscosity, the horizontal background eddy viscosity and last the effective height. The influence of the four parameters was, however, only determined for one point (just before the patch) and for one specific set of field variables (2448 individuals/m^2 and 0.2m/s). Nevertheless, in order to get a better understanding in the behaviour of the processes as result of the changing parameter values, both more observation points and different experimental settings could give better predictions for the influence on the whole system.

During the analysis of the measurement results, a discrepancy was noticed at the upper part of the vertical velocity profiles. It was assumed that the discrepancy was caused by the conveyor belt system, which creates a package of water that is not brought into movement properly. Therefore, a new calibration parameter was introduced: the 'effective height'. Relating the conveyor belt to the discrepancy, however, is rather questionable. Although the model results for implementing the effective height as a calibration parameter are reasonably accurate, the discrepancy could be caused by a totally different source.

8.1.6 Calibration

During the calibration period, the model results were compared with the measurement data by varying four parameters. As result of the narrowing-down approach (like focussing binoculars) the model results appear to be relatively well comparable. This process, however, has been done on a trial-and-error based approach, since the implementation for automatically running a script (e.g. a Matlab-based objective function script) could not be applied on Delft3D. If a script for automatically running the model for different parameter sets can be written, then the 'optical' parameter set could be determined

straightforwardly. When using objective functions, Pareto fronts could be created followed by indicating the range of the objective parameter. This however will be too time consuming, even with a small model used in this study. Therefore, when investigating relating subjects to this study, under the condition that sufficient knowledge on the subject is obtained, the trial-and-error method is recommended. The time consumed when using an automatically script, might be used in a more constructive way e.g. applying a finer grid.

Like described above, the results of the calibration process for using four calibration parameters are rather comparable with the measurement data. For a more accurate approximation of the measurement data, more calibration parameters could be introduced. Nevertheless, like described in the discussion on the govern equations, using significant more calibration parameters could cause overparameterization. In this situation, the obtained 'optimal' parameter sets are useless, since it is ambiguous which parameter sets should be applied on further studies.

In the calibration process, both the simulated data and the flume data were averaged. The modelled data was averaged in order to obtain the data on the correct distance from the patch. The flume data was averaged in order to correct for possible discrepancies caused by local processes. In both averaging processes, in influences of the on-going processes on the velocity profiles are flattened. The advantage of this process is that only information on the main processes is maintained. The main disadvantage, however, is that the information on the spatial distribution of these main processes, which is very useful in prediction of sediment-erosion patterns, is lost. Moreover, this could have a significant effect on the reliability of the final calibration parameter values.

In a good model the calibration process is followed by a validation period. More data should be acquired in order to provide sufficient data for the validation process of the results of this study. Of course, one could argue that using the same calibration values for different settings is already a validation. Validation of the obtained parameter set in totally other settings (i.e. other flume experiments or field data) could give more information on the correctness of the final calibrated parameter values.

8.1.7 Implementation

In the implementation process of this study, the influences of three different field variables on the bed shear stress patterns is tested, when applying the final calibrated parameter values on the hydrodynamic model. These influences on the bed shear stress patterns are tested with help of a self-created formula. However this is not an existing formula, it is believed this equation can provide useful information on the bed shear stress patterns created by different scenarios.

With help of this self-created equation, the influence of three different field variables on the bed shear stress in investigated. Of course, applying more variables could cover more different scenarios. Using 'only' three field variables in order to create different scenarios, however, will enhance the possibility of relating the overall influence to their influence on the bad shear stress patterns.

Finally, for each field variable extreme values have been used in order to determine the scenarios that were used during the implementation process. However these extreme values do not cover the total variability of the field variables, it is believed that the developed scenarios will provide sufficient information on the influences on the bed shear stress patterns.

8.2 Discussion on the results

8.2.1 Measurements

Despite of the fact the flume experiment were time-consuming, the measurement data showed comparable results with the background theory and other studies. For the largest flow velocity (0.20 m/s), however, there appeared to be an inconsistency with the theory. In the upper part of the vertical velocity profiles a discrepancy was noticed. As described in Chapter 5, it was assumed that the inconsistency was caused by the conveyor belt system, which created a package of water that was not brought into movement properly. Although this assumption of relation the conveyor belt to the inconsistency is rather questionable, the model results for taking into account this discrepancy (by implementing effective height as a calibration parameter) are reasonably accurate with the flume data.

In the theory, the stabilizing effect of a patch, which is caused by the patch in total, is described extensively. Nevertheless, in these stabilizing patches, there are still some on-going destabilizing processes present. Local high turbulence levels near the piles could cause discrepancies in the observed velocity profiles. Despite the fact that these processes are very local, their influences on the velocity profiles have been observed during the flume measurements.

8.2.2 Sensitivity analysis

In former studies (Friedrichs et al., 2000; Bouma et al., 2007 (vegetation); Borsje et al., 2009a,b), the hydrodynamic and sediment dynamic processes within the patches of vegetation and benthos are described extensively. The processes modelled in this thesis correspond qualitatively well with the flow behaviour described in these studies. It should be noted that the results of this part might not be totally correct due to the fact that the final calibration parameter setting has not been implemented yet in the sensitivity analysis. Therefore, in this part only a qualitative analysis is made. The quantitative comparison of the model results with former studies is described in the calibration part.

In the velocity profiles four patterns emerged, which corresponds with the studies mentioned above: deceleration within the patch, acceleration above the patch, uplift in front of the patch and, finally, horizontal acceleration in front of the patch. All these patterns reacted as expected according the background theory to the changing field parameters.

The turbulent kinetic energy patterns caused by the patch correspond relatively well with the results from formers studies (Friedrichs et al., 2000; Bouma et al., 2007 (vegetation)). For more extreme parameter settings (e.g. higher patch densities and higher flow velocities), the maximum in turbulent kinetic energy shifts towards the front and the top of the patch. In these extreme settings, the total area of the generated turbulent kinetic energy increases. The area, where high turbulent energy levels are created, however, decreases for these extreme settings.

In recent studies (Friedrichs et al., 2000; Bouma et al., 2007 (vegetation); Borsje et al., 2009a,b), the bed shear stress profiles are determined in order to give realistic statements about the erosion and sedimentation processes. In front of the patch the highest bed shear stresses occur, while within the patch the lowest bed shear stress levels arise. Since the patch is almost 2.5 meter long and therefore outweighs the horizontal grid, the lowest bed shear stress levels are rather accurate. The bed shear stress maximum, however, occurs on a smaller scale than the horizontal grid. Therefore, the accuracy of the maximum stress is rather questionable.

8.2.3 Calibration

The calibration results are rather comparable with the flume data. There are, however, some differences between the results from the calibration and the results from the measurements. For the flow velocity of 0.1 m/s, the hydrodynamic model overestimates the flume data up to 10%. This discrepancy was assumed to be caused by the conveyor belt system, which could create a package of water that is not brought into movement properly. Although relating this source to the discrepancy is rather doubtful, implementing the 'effective height' as a new calibration parameter improved the model results relatively a lot (from almost 100% overestimation to 10% overestimation).

Compared with former studies with the same parameter settings (i.e. ~3000 ind./m^2, 0.05-0.10 m/s), the reduction of the near-bottom velocity as result of the patch seems to be rather small: 20% reduction compared with a reduction of almost 70% (Friedrichs et al., 2000). Nevertheless, the velocity profiles provided by the model are obtained at the upstream edge of the patch, while the results from the work of Friedrichs et al. (2000) are obtained at almost 30 cm downstream of the edge. At the latter distance downstream of the edge the influencing patterns are completely developed, which result in a smaller reduction of the near-bottom velocity.

8.2.4 Implementation

Since there is less information on the bed shear stress variations as result of the patches available, the results can only be compared with flume measurements and other model simulations. In the most extreme scenario, the maximum bed shear stress upstream of the patch can be up to 60% higher than in the case of no patch of tube building worms. In a model research on underwater nourishments of Borsje et al. (2010), the increase in bed shear stress in only 20%. The difference in maximum bed shear stress levels is probably caused by the extreme scenarios that are used in this thesis, while in the study of Borsje et al. (2010) a water column of 2 m, a flow velocity of 0.2 m/s and a density of 2000 ind./m^2 are used.

The reduction in bed shear stress levels is more comparable with the results of the study of Borsje et al. (2010). In the most extreme scenario, a decrease in bed shear stress of more than 90% is noticed, while in the reference study a reduction of almost 85 % is observed. Remarkably, the patch appears to have a stabilizing effect already at 1000 ind./m^2. However former studies (e.g. Friedrichs et al., 2000) show that skimming flow can occur at 5% area coverage, in field conditions the stabilizing effect of the tube building worms might occur at even lower densities viz. 2% area coverage.

Furthermore, the pattern that for less extreme scenarios the contribution of the patch density increase emerges. However, when going from scenario 2 to scenario 1, a small decrease in the scaled maximum bed shear stress is observed. This decreasing pattern cannot be explained by the background theory. It is believed that the grid, which is too coarse to give a good quantitative representation of the maximum bed shear stress, is responsible for this decrease in scaled maximum bed shear stress.

9 Conclusions and recommendations

9.1 Conclusions

9.1.1 Biophysical interactions

In determining the influences of the biophysical interactions of the tube building worms with the flow, the discipline biogeomorphology describes the important processes. In biogeomorphology, a combination of geomorphology and ecology (Viles, 1998), knowledge of the shear stresses is of great importance, as these stresses are the driving force behind the erosion and sedimentation processes (De Jong, 2005). Furthermore, Hulscher (1996) mentioned that bed load transport is the dominant type of sediment transport in offshore tidal regimes, like the North Sea.

Elements, like tube building worms, can by interacting with the flow have both stabilizing and destabilizing effects on the sediment dynamics, depending on the flow characteristics and the density of tube building worms. In the most extreme scenario, skimming flow may occur. In this situation, the elements are relatively so close together and hinder flow to such a degree, that the main body of water passes over them instead of through them and causing the flow to skim over the tops of the elements (Gordon et al, 2004). The entire flow profile is displaced upward and thereby preventing sediment from the bed to erode (Eckman et al., 1981). In several studies (Friedrichs et al., 2000; Bouma et al., 2007; Friedrichs and Graf, 2009; Peine et al., 2009; Friedrichs et al., 2009) skimming flow behaviour has already been observed at low densities of 5% area coverage.

One way to determine the bottom shear stress is to use the relation between turbulence and bed shear stress (Soulsby and Dyer, 1981; Kim et al., 2000; and Pope et al., 2006). The conditions when bed particle starts to move are described by Liu (1999):

- When the friction velocity exceeds the critical friction velocity,

- When the bed shear stress exceeds the critical bed shear stress,

- When the Shields parameter exceeds the critical Shields parameter.

Now, the sediment transport can be calculated by the equation of Van der Veen et al. 2006 (based on earlier work of Hulscher 1996), which describes the relation between bed shear stress and bed load transport.

9.1.2 Hydrodynamic model Delft3D

9.1.2.1 Govern equations

In this thesis, the FLOW-module of the three-dimensional hydrodynamic model Delft3D (Deltares, 2009), which computes flow characteristics (flow velocity, turbulence) dynamically in time over a three-dimensional spatial grid, was used. Delft3D-FLOW is a numerical model based finite differences covered by a staggered grid, which uses an alternating direction implicit (ADI) time integration method to solve the continuity and horizontal momentum equations (Lesser et al., 2004).

However wave-flow interactions were neglected, the many processes included in the FLOW-module make it capable of 3D simulations of ocean basins, coastal seas and rivers, etc. (Lesser, 2004). Beside the continuity and horizontal momentum equations, Delft3D uses a turbulence closure model. Although the

influences on the bed shear stress were examined, the transport module was not used since this study was time-bounded.

In order to solve the equations above a turbulence closure model is needed. The used hydrodynamic grid was too coarse and the time steps too large to resolve the turbulent scales of motion in these equations, i.e. the turbulent processes were "sub-grid" (Deltares, 2009). The simplest turbulence closure model suitable for modelling the flow through elements, like patches of tube building worms, is the *k-ε* turbulence model (Uittenbogaard, 2003). In the *k-ε* turbulence closure model both the turbulent energy *k* and the dissipation *ε* are produced by production terms representing shear stresses at the bed, surface, and in the flow (Lesser et al., 2004).

9.1.2.2 Flow-element interaction
The difference of the model used with the standard version of Delft3D is the inclusion of the effect of the tube building worms on the flow and that it explicitly account for the influence of rigid cylindrical structures, like tube building worms, on the drag and turbulence (Uittenbogaard, 2003). The translation of the elements into the model was done by the so-called vegetation rod-module. Lastly, a schematized two-dimensional vertical (2DV) model is used to reduce costly computation time.

The k-ε model is relatively simple to implement, it leads to stable calculations, and it converges relatively easily (Biswas and Eswaran, 2002). There could, however, be some improvements on the model itself. First of all, the dissipation equation is rather simplistic. This could be solved by introducing equations instead of the simple model parameters. Nevertheless, the disadvantage of this method is that it could lead to overparameterization. Furthermore, the pressure correction technique could be used in order to compensate for neglecting the vertical accelerations. Finally, before up-scaling the flume experiments to field conditions, the following processes have to be implemented into the model: the wave-flow interactions, the flow-sediment interactions, the changing benthic variability and the Coriolis force.

9.1.3 Calibration

9.1.3.1 Measurements
Two 'identical' situations, viz. a flume tank experiment and a three-dimensional hydrodynamic model, were created to test the predictive power of the model. Thin (equal) piles were distributed randomly with a fixed height over a grid in the flume. By changing the patch density (i.e. the number of tubes per m^2) and the flow velocity, different settings were created to calibrate the model on.

Although the processes that have not been taken into consideration were minimized, not all undesired influences can be neglected. The side walls could cause some extra turbulence creation and additional energy dissipation at the side walls. In general, turbulence intensities observed in the flume are lower than in the field and the flume tank dimensions determine the largest eddy sizes (Bouma et al., 2007). Furthermore, vertical accelerations were neglected, while in front of the patch the flow is changed abruptly into the vertical direction.

The influences of these patterns is however not clear, so the effect of taking into account these pattern should be investigated. For the vertical acceleration, it is believed that applying the pressure correction technique (Casulli (1999) and Busnelli (2001)) for computing the non-hydrostatic pressure gives reasonable results.

9.1.3.2 Sensitivity analysis and calibration

In order to calibrate the model by the flume measurements, a sensitivity analysis was executed to determine the behaviour of the model as result of changing field parameters. In this study, the influence of four parameters on the hydrodynamics and sediment dynamics was examined. The four parameters, that were investigated, are the (Chézy) roughness coefficient, the vertical background eddy viscosity, the horizontal background eddy viscosity and the 'effective' height. The latter parameter was introduced in order to minimize the discrepancies, which might be caused by a not-properly working conveyor belt system. More calibration parameter could be introduced. Nevertheless, too many parameters could cause overparameterization.

In the calibration process, both the simulated data and the flume data were averaged. The modelled data was averaged in order to obtain the data on the correct distance from the patch. The flume data was averaged in order to correct for possible discrepancies caused by local processes.

The calibrated model provides a realistic representation of the actual velocity profiles. Despite of the relatively accurate approximation of the simulation, there are still some deviations. Since the deviations are the smallest for the highest flow velocities (i.e. 0.2 m/s), which are comparable with typical North Sea circumstances, it is believed that the simulations provide a realistic impression of the near-bottom flow and therefore a realistic impression of the bed shear stress. Moreover, the discrepancies in the velocity profiles are realistic compared to other studies (Bouma et al., 2007). Validation of the obtained parameter set in totally different settings could give more information on the correctness of the final calibrated parameter values.

In order to increase the predictive value of the model, both the quantity and the quality of the data should be increased. More data allows the model to be validated on. Increasing the quality of the data should focus on determining the source of the discrepancies. Now, it is assumed that the conveyor belt system is responsible for the deviations. This assumption, however, is rather questionable. Furthermore, an automatically running script (instead of a trial-and-error based approach) could improve the calibration method a lot. This process is, however, very time consuming.

9.1.4 Implementation

In the implementation process, the influences of three different field variables (viz. the water depth, the flow velocity and the patch density) on the bed shear stress were tested, when applying the final parameter set. These influences on the bed shear stress we investigated with use of a self-created relation and scenarios. Although the used scenarios do not cover the total diversity of the field variables, it is believed that the developed scenarios provide sufficient information on the influences on the bed shear stress patterns.

From the implementation process some interesting result emerged. For more extreme situations, the bed shear stress increases rapidly compared to a situation of no occurrence of tube building worms. Upstream of the patch an increase of almost 60% is observed. Within the patch a reduction in bed shear stress levels of at least 80% is noticed. When scaling the bed shear stress levels with the case there are no tube building worms present, these patterns cannot be detected. Now, in more extreme scenarios, the scaled bed shear stress levels decrease before the patch and increase within the patch. This might indicate on less influencing effects of the tube building worms for more extreme situations i.e. for more extreme situations the sedimentation patterns decrease and could even shift to erosion patterns.

Remarkable, however, in the patterns for the scaled bed shear stress, is the small reduction in the scaled maximum bed shear stress when going from scenario 2 to scenario 1. A possible cause for this decrease is the scale of the grid. In this situation, the grid scale (15 cm) is too coarse to give a realistic representation of the maximum bed shear stress (30-50 cm).

9.1.5 Flume vs. field

For up-scaling flume experiments tot field condition, some assumptions were made. The link between flume and field conditions is, however, not so straightforward. Although former work has indicated that the flow patterns found in the NIOO flume tank are comparable to situations of steady flow in the field (Hendriks et al., 2006), flow in flume tanks is always at best an idealized representation of flow in the field. In the field, neither all the tubes have the same height and diameter, nor are they distributed spatially uniform. Furthermore, in the flume tank the flow is not able to flow around the patch.

9.2 Recommendations

- Delft3D provides a suitable flow-module to model three dimensional hydrodynamic processes that occur in coastal seas. In offshore tidal regimes, like the North Sea, however, wave-flow and flow-transport interaction occur. Therefore, for up-scaling flume experiments to field condition, wave-flow interactions, flow-sediment interactions, the changing benthic variability and the Coriolis force should be implemented into a 3D (instead of a 2DV) hydrodynamic grid. Furthermore, the influences of implementing the pressure correction technique should be investigated.

- Since the turbulent processes are usually sub-grid, a turbulence closure model is needed. With the k-ε turbulence closure model, Delft3D provides a suitable model for simulating flow through patches of tube building worms. As the model performs reasonably accurate, and given that the computing time should be minimized as much as possible, it is believed that the appropriate k-ε model should be used for modelling flow through elements.

- For the measurement, the influences of the side walls of the flume on the hydrodynamic behaviour should be examined.

- The quality of the data should be increased, with the focus on determining the source of the discrepancies. The source of the discrepancies found at the calibration part should be investigated and, if possible, the discrepancies should be minimized.

- A validation process of the obtained final parameter set in totally different setting should provide more information on the correctness of the parameter set and the model. For this process, also more data should be acquired.

- The horizontal grid, especially in front of the grid, should be finer in order to get a better qualitative data and model results in velocity and bed shear stress profiles.

- If possible, an automatically running script should be developed to make the calibration process more scientific.

- The influence of implementing more calibration variables (e.g. variables instead of turbulence closure constants or background diffusivity) should be investigated. There should, however, be awareness on the fact that overparameterization could occur.

- For the implementation period, more scenarios could be developed in order to get more detailed information of the bed shear stress variability.

10 Literature

Baptist, M. (2005). Modelling floodplain biogeomorphology, Delft University of Technology.

Baptist, M.J., J. E. Tamis, B.W. Borsje, J.J. van der Werf (2009). Review of the geomorphological, benthic ecological and biogeomorphological effects of nourishments on the shoreface and surf zone of the Dutch coast, IMARES, Deltares.

Biswas, G. and V. Eswaram (2002). " Turbulent Flows – Fundamentals, Experiments and Modeling." Narosa Publishing House

Bobertz, B., J. Harff, et al. (2009). "Parameterisation of clastic sediments including benthic structures." Journal of Marine Systems **75**(3-4): 371-381.

Borsje, B.W., M. A. Kruijt., Jebbe J. van der Werf, Suzanne J.M.H. Hulscher, and P. M. J. Herman (2010). "Modeling biogeomorphological interactions in underwater nourishments." Coastal engineering.

Borsje, B. W., M. B. de Vries, et al. (2009). "Modeling bio-geomorphological influences for offshore sandwaves." Continental Shelf Research **29**(9): 1289-1301.

Borsje, B. W., S. J. M. H. Hulscher, et al. (2009). "On the parameterization of biological influences on offshore sand wave dynamics." Ocean Dynamics **59**(5): 659-670.

Borsje, B.W., Hulscher, S.J.M.H., Herman, P.M.J. (2011). "Exploring bio-physical interactions in tube building worm fieldscombining model and flume experiments". PhD progress talk.

Bosch, L. v. d. (2003). Influence of vegetation on flow and morphology in the river Allier, France, Delft University of Technology.

Bouma, T. J., L. A. van Duren, et al. (2007). "Spatial flow and sedimentation patterns within patches of epibenthic structures: Combining field, flume and modelling experiments." Continental Shelf Research **27**(8): 1020-1045.

Bouma, T.J., M. B. de Vries, E. Low, G. Peralta, I. C. Ta´ nczos, J. Van de koppel, and P. M. J. Herman (2005). "Trade-offs related to ecosystem engineering: a case study on stiffness of emerging macrophytes." Ecology **86**(8): 2187–2199.

Deltares, 2009. User manual Delft-3D FLOW, Deltares (www.deltares.nl), Delft, The Netherlands.

Eckman, J.E. , A. R. M. Nowell, P.A. Jumars (1981). "Sediment destabilization by animal tubes." Journal of Marine Research **39**(2).

Folkard, A. M. (2010). "Flow regimes in gaps within stands of flexible vegetation: laboratory flume simulations." Environmental Fluid Mechanics **11**(3): 289-306.

Friedrichs, M., G. Graf, B. Springer (2000). "Skimming flow induced over a simulated polychaete tube lawn at low population densities." Marine ecology progress series **192**: 219-228.

Friedrichs, M. and G. Graf (2009). "Characteristic flow patterns generated by macrozoobenthic structures." Journal of Marine Systems **75**(3-4): 348-359.

Friedrichs, M., T. Leipe, et al. (2009). "Impact of macrozoobenthic structures on near-bed sediment fluxes." Journal of Marine Systems **75**(3-4): 336-347.

Hendriks, I. E., L. A. van Duren, et al. (2006). "Turbulence levels in a flume compared to the field: Implications for larval settlement studies." Journal of Sea Research **55**(1): 15-29.

Hoogduin, L. (2009). Sediment transport through the eastern scheldt storm surge barrier, Delft University of Technology.

Jacobs, W. (2004). Modelling the Rhine River Plume, Delft University of Technology.

Jong, J. de (2005). Modelling the influence of vegetation on the morphodynamics of the river Allier, Delft University of Technology.

Godet, L., N. Toupoint, Fre´de´ ric Olivier, Jerome Fournier and Christian Retiere (2008). "Considering the Functional Value of Common Marine Species as a Conservation Stake: The Case of Sandmason Worm Lanice conchilega (Pallas 1766) (Annelida, Polychaeta) Beds." Ambio **37**(5).

Gordon N.D*., McMahon T.A. & Finlayson B.L. (*1992*) Stream Hydrology: an Introduction for Ecologists. Wiley, Chichester,* 139 *p.*

Lesser, G. R., J. A. Roelvink, et al. (2004). "Development and validation of a three-dimensional morphological model." Coastal Engineering **51**(8-9): 883-915.

Liek, G. A. (2000). Horizontal large eddy simulation using Delft2D-MOR, Delft University of Technology.

Liu, Z. (2001). Sediment transport. Aalborg, Laboratoriet for Hydraulik og Havnebygning, Instituttet for Vand, Jord og Miljøteknik, Aalborg Universitet.

Morris, H.M. (1955). Flow in rough conduits. *Trans. ASCE* **120**: 373-398.

Neumeier, U. (2007). "Velocity and turbulence variations at the edge of saltmarshes." Continental Shelf Research **27**(8): 1046-1059.

Neumeier, U. R. S. and C. L. Amos (2006). "The influence of vegetation on turbulence and flow velocities in European salt-marshes." Sedimentology **53**(2): 259-277.

Parson, A.J., Abrahams, A.D. (2009). "Geomorphology of Desert Environments, Second Edition". *Springer Netherlands,* , 38 p.

Peine, F., M. Friedrichs, et al. (2009). "Potential influence of tubicolous worms on the bottom roughness length z0 in the south-western Baltic Sea." Journal of Experimental Marine Biology and Ecology **374**(1): 1-11.

Rabaut, M., K. Guilini, et al. (2007). "A bio-engineered soft-bottom environment: The impact of Lanice conchilega on the benthic species-specific densities and community structure." Estuarine, Coastal and Shelf Science **75**(4): 525-536.

Ronde, J.G. de, J. P. M. Mulder. R. Spanhoff (2003). Morphological developments and coastal zone management in the netherlands. International Conference on Estuaries and Coasts. Hangzhou, China, National Institute for Coastal and Marine Management/RIKZ, Rijkswaterstaat.

Temmerman, S., T. J. Bouma, et al. (2005). "Impact of vegetation on flow routing and sedimentation patterns: Three-dimensional modeling for a tidal marsh." Journal of Geophysical Research **110**(F4).

Uittenbogaard, R. (2003). Modelling turbulence in vegetated aquatic flows.

Vries, M. de, T. Bouma, M. van Katwijk, B. Borsje en B. van Wesenbeeck (2007). Biobouwers van de Kust, Rijkswaterstaat WaterINNovatiebron.

Wolfe, S.A. and W.G. Nickling (1993). 'The protective role of sparse vegetation in wind erosion', Progress in Physical Geography, **17**, 50–68.

11 List of figures

12 List of tables

13 Appendix 1 – Grid specifications

Table 13-1 – The dimensions of the vertical grid with the cells where the patch is located highlighted in light blue.
* = z-coordinate of the lower boundary is indicated.

Vertical Grid							
Cell	Δz (%)	Δz (mm)	z-coor. (mm)*		Cell	Δz (%)	Δz (mm)	z-coor. (mm)*
1	2.50	10.00	390.00		36	0.35	1.40	35.40
2	10.00	40.00	350.00		37	0.35	1.40	34.00
3	10.00	40.00	310.00		38	0.35	1.40	32.60
4	7.50	30.00	280.00		39	0.35	1.40	31.20
5	7.50	30.00	250.00		40	0.35	1.40	29.80
6	5.00	20.00	230.00		41	0.35	1.40	28.40
7	5.06	20.25	209.75		42	0.35	1.40	27.00
8	4.00	16.00	193.75		43	0.35	1.40	25.60
9	3.13	12.50	181.25		44	0.30	1.20	24.40
10	3.00	12.00	169.25		45	0.30	1.20	23.20
11	2.75	11.00	158.25		46	0.30	1.20	22.00
12	2.50	10.00	148.25		47	0.30	1.20	20.80
13	2.50	10.00	138.25		48	0.30	1.20	19.60
14	2.31	9.25	129.00		49	0.30	1.20	18.40
15	2.00	8.00	121.00		50	0.30	1.20	17.20
16	2.20	8.80	112.20		51	0.28	1.10	16.10
17	2.10	8.40	103.80		52	0.28	1.10	15.00
18	1.90	7.60	96.20		53	0.25	1.00	14.00
19	1.70	6.80	89.40		54	0.25	1.00	13.00
20	1.60	6.40	83.00		55	0.25	1.00	12.00
21	1.40	5.60	77.40		56	0.23	0.90	11.10
22	1.20	4.80	72.60		57	0.23	0.90	10.20
23	1.05	4.20	68.40		58	0.23	0.90	9.30
24	1.00	4.00	64.40		59	0.23	0.90	8.40
25	0.95	3.80	60.60		60	0.22	0.86	7.54
26	0.80	3.20	57.40		61	0.22	0.86	6.68
27	0.80	3.20	54.20		62	0.22	0.86	5.82
28	0.70	2.80	51.40		63	0.22	0.86	4.96
29	0.70	2.80	48.60		64	0.22	0.86	4.10
30	0.60	2.40	46.20		65	0.22	0.86	3.24
31	0.60	2.40	43.80		66	0.20	0.80	2.44
32	0.50	2.00	41.80		67	0.20	0.80	1.64
33	0.50	2.00	39.80		68	0.15	0.60	1.04
34	0.40	1.60	38.20		69	0.15	0.60	0.44
35	0.35	1.40	36.80		70	0.11	0.44	0.00

Table 13-2 – The dimensions of the horizontal grid with the cells where the patch is located highlighted in light blue. * = x-coordinate of the South-boundary is indicated.

Horizontal grid

Cell	x-coor. (m)	*Δx (m)	Cell	x-coor. (m)	*Δx (m)	Cell	x-coor. (m)	*Δx (m)	Cell	x-coor. (m)	*Δx (m)
1	100.0	0.60	41	118.0	0.30	81	125.50	0.15	121	133.0	0.30
2	100.6	0.60	42	118.3	0.30	82	125.65	0.15	122	133.3	0.30
3	101.2	0.60	43	118.6	0.30	83	125.80	0.15	123	133.6	0.30
4	101.8	0.60	44	118.9	0.30	84	125.95	0.15	124	133.9	0.30
5	102.4	0.60	45	119.2	0.30	85	126.10	0.15	125	134.2	0.30
6	103.0	0.60	46	119.5	0.29	86	126.3	0.15	126	134.5	0.30
7	103.6	0.60	47	119.8	0.29	87	126.4	0.15	127	134.8	0.30
8	104.2	0.60	48	120.1	0.27	88	126.6	0.15	128	135.1	0.30
9	104.8	0.60	49	120.3	0.25	89	126.7	0.15	129	135.4	0.30
10	105.4	0.60	50	120.6	0.23	90	126.8	0.15	130	135.7	0.30
11	106.0	0.60	51	120.8	0.21	91	127.0	0.15	131	136.0	0.30
12	106.6	0.60	52	121.1	0.19	92	127.2	0.15	132	136.3	0.30
13	107.2	0.60	53	121.2	0.18	93	127.3	0.15	133	136.6	0.30
14	107.8	0.60	54	121.4	0.17	94	127.4	0.15	134	136.9	0.30
15	108.4	0.60	55	121.6	0.16	95	127.6	0.15	135	137.2	0.30
16	109.0	0.60	56	121.7	0.15	96	127.7	0.15	136	137.5	0.31
17	109.6	0.57	57	121.9	0.15	97	127.9	0.15	137	137.8	0.32
18	110.2	0.56	58	122.0	0.15	98	128.0	0.15	138	138.1	0.34
19	110.7	0.52	59	122.2	0.15	99	128.2	0.15	139	138.5	0.38
20	111.3	0.48	60	122.4	0.15	100	128.4	0.15	140	138.8	0.42
21	111.7	0.42	61	122.5	0.15	101	128.5	0.15	141	139.3	0.46
22	112.2	0.38	62	122.6	0.15	102	128.7	0.15	142	139.7	0.49
23	112.5	0.34	63	122.8	0.15	103	128.8	0.15	143	140.2	0.58
24	112.9	0.32	64	122.9	0.15	104	129.0	0.15	144	140.8	0.60
25	113.2	0.31	65	123.1	0.15	105	129.1	0.15	145	141.4	0.60
26	113.5	0.30	66	123.3	0.15	106	129.3	0.15	146	142.0	0.60
27	113.8	0.30	67	123.4	0.15	107	129.4	0.16	147	142.6	0.60
28	114.1	0.30	68	123.6	0.15	108	129.6	0.17	148	143.2	0.60
29	114.4	0.29	69	123.7	0.15	109	129.7	0.19	149	143.8	0.60
30	114.7	0.31	70	123.85	0.15	110	129.9	0.21	150	144.4	0.60
31	115.0	0.32	71	124.00	0.15	111	130.1	0.24	151	145.0	0.60
32	115.3	0.28	72	124.15	0.15	112	130.4	0.26	152	145.6	0.60
33	115.6	0.30	73	124.30	0.15	113	130.6	0.28	153	146.2	0.60
34	115.9	0.30	74	124.45	0.15	114	130.9	0.29	154	146.8	0.60
35	116.2	0.30	75	124.60	0.15	115	131.2	0.30	155	147.4	0.60
36	116.5	0.30	76	124.75	0.15	116	131.5	0.30	156	148.0	0.60
37	116.8	0.30	77	124.90	0.15	117	131.8	0.30	157	148.6	0.60
38	117.1	0.30	78	125.05	0.15	118	132.1	0.30	158	149.2	0.60
39	117.4	0.30	79	125.20	0.15	119	132.4	0.30	159	149.8	0.60
40	117.7	0.30	80	125.35	0.15	120	132.7	0.30			

14 Appendix 2 – Extensive description Delft3D-FLOW

In this part the full description of the terms, that emerge in the govern equations used by Delft3D-FLOW, is given. Furthermore, a description of the used boundary conditions, the vegetation-rod module and the numerical aspects is given.

14.1 Terms govern equations

The production term, where the horizontal gradients of the horizontal velocity and all the gradients of the vertical velocities are neglected, is given by,

$$P_k = \nu_V \left(\left(\frac{\partial u}{\partial z} \right)^2 + \left(\frac{\partial v}{\partial z} \right)^2 \right). \tag{47}$$

The buoyancy flux, B_k, represents the conversion of turbulent kinetic energy into potential energy, with $\sigma_\rho = 0.7$ according to:

$$B_k = g \frac{\nu_{3D}}{\rho \sigma_\rho} \frac{\partial \rho}{\partial z}. \tag{48}$$

The relation between the energy dissipation ε the turbulent kinetic energy k is assumed to be a function depended on the mixing length L and the calibration constant c_D:

$$\varepsilon = c_D \frac{k\sqrt{k}}{L} \tag{49}$$

The last three terms in the energy dissipation equation, the production term of the energy dissipation P_ε, the buoyancy flux B_k, and the dissipation of the dissipation ε_ε, are respectively given by,

$$P_\varepsilon = c_{1\varepsilon} \frac{\varepsilon}{k} P_k , \tag{50}$$

$$B_\varepsilon = c_{1\varepsilon} \frac{\varepsilon}{k} (1 - c_{3\varepsilon}) B_k , \tag{51}$$

$$\varepsilon_\varepsilon = c_{2\varepsilon} \frac{\varepsilon^2}{k}. \tag{52}$$

with $c_{1\varepsilon} = 1.44$, $c_{2\varepsilon} = 1.92$ and $c_{3\varepsilon} = 1.0$.

Now, the equation to determine the eddy viscosity becomes:

$$\begin{aligned} \nu_V &= c'_\mu L\sqrt{k} \\ &= c_\mu \frac{k^2}{\varepsilon} , \end{aligned} \tag{53}$$

with $c_\mu = c'_\mu c_D = 0.09$.

14.2 Boundary conditions

14.2.1 Kinematic boundary conditions

To solve the set of differential equations, the following boundary conditions are required. The kinematic boundary conditions at the bed (z = -b) and at the free surface (z = ζ) are given by,

$$w|_{z=\zeta} = \frac{\partial \zeta}{\partial t} + u\frac{\partial \zeta}{\partial x} + v\frac{\partial \zeta}{\partial y} = 0 \,, \tag{54}$$

$$w|_{z=-b} = u\frac{\partial b}{\partial x} + v\frac{\partial b}{\partial y} = 0 \,. \tag{55}$$

As described above, the water surface elevation ζ varies in time with x and y. Integrating the continuity equation over depth and using kinematic boundary conditions from above leads to the free surface equation,

$$\frac{\partial \zeta}{\partial t} + \frac{\partial}{\partial x}\int_{-b}^{\zeta} u dz + \frac{\partial}{\partial y}\int_{-b}^{\zeta} v dz = 0 \,. \tag{56}$$

14.2.2 Free surface boundary conditions

At the free surface, the boundary conditions for the momentum equations and the transport equations are respectively:

$$\nu_V \frac{\partial u}{\partial z}\bigg|_{z=0} = 0 \,, \tag{57}$$

$$\nu_V \frac{\partial v}{\partial z}\bigg|_{z=0} = 0 \,, \tag{58}$$

$$k|_{z=0} = 0 \,, \tag{59}$$

$$\varepsilon|_{z=0} = 0 \,. \tag{60}$$

14.2.3 Bed boundary conditions

At the seabed, the boundary conditions for the momentum equations and the transport equations are respectively:

$$\nu_V \frac{\partial u}{\partial z}\bigg|_{z=-d} = \frac{\tau_{bx}}{\rho_0} \,, \tag{61}$$

$$\nu_V \frac{\partial v}{\partial z}\bigg|_{z=-d} = \frac{\tau_{by}}{\rho_0} \,, \tag{62}$$

$$k|_{z=-d} = \frac{u_{*b}^2}{\sqrt{c_\mu}} \,, \tag{63}$$

$$\varepsilon|_{z=-d} = \frac{u_{*b}^3}{\kappa z_0}. \tag{64}$$

where τ_{bx} and τ_{by} are the components of the bed stress in x- and y-direction respectively. u_{*b} is the friction velocity determined from the magnitude of the velocity in the bed's nearest grid point and κ is the Von Kármáns constant, $\kappa \approx 0.41$.

14.3 3D-vegetation-model

The 3D-model presented by Baptist (2005) gives an implantation of the 1-DV model of Uittenbogaard (2003) into the shallow-water equations, which is mainly focused on the vertical derivatives of horizontal velocities. In this model there is an essential inclusion of the porosity $(1 - \lambda)$ in the description of the vertical momentum exchange and the vertical diffusion of the $k-\varepsilon$ equations.

With this implementation the horizontal momentum equations, without the Coriolis force and the density-driven stratification, for a hydrostatic pressure assumption, read:

$$\frac{\partial u}{\partial t} + u\frac{\partial u}{\partial x} + v\frac{\partial u}{\partial y} + w\frac{\partial u}{\partial z} + g\frac{\partial \zeta}{\partial x}$$
$$= \frac{1}{1-\lambda}\frac{\partial}{\partial z}\left((1-\lambda)\nu_V\frac{\partial u}{\partial z}\right) + \frac{\partial R_{xx}}{\partial x} + \frac{\partial R_{xy}}{\partial y} - \frac{F_u}{1-\lambda}, \tag{65}$$

$$\frac{\partial v}{\partial t} + u\frac{\partial v}{\partial x} + v\frac{\partial v}{\partial y} + w\frac{\partial v}{\partial z} + g\frac{\partial \zeta}{\partial y}$$
$$= \frac{1}{1-\lambda}\frac{\partial}{\partial z}\left((1-\lambda)\nu_V\frac{\partial v}{\partial z}\right) + \frac{\partial R_{xy}}{\partial x} + \frac{\partial R_{yy}}{\partial y} - \frac{F_v}{1-\lambda}, \tag{66}$$

in which the normal stress components (divided by fluid density) are according to:

$$R_{xx} = 2(\nu + \nu_V + \nu_H)\frac{\partial u}{\partial x} \tag{67}$$

$$R_{yy} = 2(\nu + \nu_V + \nu_H)\frac{\partial v}{\partial y} \tag{68}$$

And the shear stress component (divided by fluid density) according to:

$$R_{xy} = (\nu + \nu_V + \nu_H)\left(\frac{\partial u}{\partial y} + \frac{\partial v}{\partial x}\right) \tag{69}$$

The equations for the production and dissipation of the turbulent kinetic energy become with this implementation, respectively:

$$\frac{\partial k}{\partial t} + u\frac{\partial k}{\partial x} + v\frac{\partial k}{\partial y} + w\frac{\partial k}{\partial z} = \frac{1}{1-\lambda}\frac{\partial}{\partial z}\left((1-\lambda)\left(\nu + \frac{\nu_V}{\sigma_k}\right)\frac{\partial k}{\partial z}\right) + T + P_k - B_k - \varepsilon \tag{70}$$

$$\frac{\partial \varepsilon}{\partial t} + u\frac{\partial \varepsilon}{\partial x} + v\frac{\partial \varepsilon}{\partial y} + w\frac{\partial \varepsilon}{\partial z} = \frac{1}{1-\lambda}\frac{\partial}{\partial z}\left((1-\lambda)\left(\nu + \frac{\nu_V}{\sigma_\varepsilon}\right)\frac{\partial \varepsilon}{\partial z}\right) + P_\varepsilon - B_\varepsilon - \varepsilon_\varepsilon + c_{2\varepsilon}\frac{T}{\tau_{eff}} \tag{71}$$

All the rest of the terms are described in Chapter 4 .

14.3.1 Translation of worms to rods

To approximate flow through the patches the so-called Delft3D vegetation rod-model is used. Like in other reports, that give realistic model results, the tube building worms have been considered as rigid cylindrical structures. Therefore, the rod-model can be described by the following two files.

In the *.pla file, the 'vegetation' type ('lanice') is describes as a collection of cylindrical structures, which have a turbulence length scale coefficient between the stems ('ClPlant') of $C_l = 0.8$. In the Vertical Plant Structure ('Vps') part their diameter and C_D as a function of the vertical co-ordinate are specified (Figure 14-1). The number of stems per m^2 of the worm fields is given by 'Lanice.dep', which is generated by a Matlab-file 'Lanice.gen' (Figure 4-6).

```
* Directional Point Model of Vegetation input file
*
[DPMVFileInformation]
   FileCreatedBy    = Bas Borsje
   FileCreationDate = 08-12-2009
   FileVersion      = 00.01
[DPMVOverall]
   ClPlant = 0.80     [ - ] Turbulence length scale coefficient between stems
   ItPlant = 50       [ - ] Number of time steps between updates of plant arrays
[Vegetation]
   Type = lanice
      *
      * height [m]    stem diameter [m]    nr of stems [-]     cd coefficient [-]
      *
   Vps  =  0            0.005                1                 1.0
   Vps  =  0.035        0.005                1                 1.0


[Area]
   VegetationType = #lanice   #       [  -  ] must match a vegetation group in this file
   NPlantsFile    = #Lanice.dep#      [  -  ] must match an existing file in dep-format
```

Figure 14-1 – The Directional Point Model of Vegetation input file give the translation from the field to the model by representing the tube building worms as rigid cylindrical structures.

```
clc
clear all
close all

i=3264;          %number of stems per m^2
ny=400;          %grids cells in m-coordinates
nx=3;            %grids cells in n-coordinates
P(:,:)= zeros(ny,nx);
P(70:85,2:2)=i; %TBW field
newdep=[[P(:,:,1),(ones(ny,1).*-999)];(ones(1,nx+1).*-999)];
save ('Lanice.dep','newdep','-ascii');
```
Figure 14-2 – The Matlab file generates the field of tube building worms by specifying the number of stems per m^2.

14.3.2 Numerical aspects

Delft3d-FLOW is a numerical model based on finite differences covered by a staggered grid (Lesser et al., 2004). The arrangement of the variables in a staggered grid, where not all quantities are defined at the same location in the numerical grid, is called the Arakawa C-grid. The water level points are defined in the centre of a grid cell (+). The velocity components, $u(-)$ and $v(|)$, are perpendicular to the grid cell

faces where they are situated (Figure 14-3 and Figure 14-4). The water depths are located at the crossings of the gridlines. Within the indicated grey area, the (m,n) co-ordinates are constant.

To solve the continuity and horizontal momentum equations Delft3D uses an alternating direction implicit (ADI) time integration method (Leendertse, 1987). The advantage of the ADI method is that water levels and velocities are implicitly coupled along grid lines. First, the equations in the *x*-direction are solved implicitly in time, while the equations in the y-direction are solved explicitly. This is followed by the same procedure in the opposite order. This leads to systems of equations with a small band width (Lesser et al, 2004).

The horizontal advection terms in the transport equation are solved using the so-called "cyclic method" (Stelling and Leendertse, 1991). This method splits the third-order upwind scheme for the first derivative into two second-order central discretizations and an upwind discretization. These discretizations are successively used in both stages of the ADI scheme (Lesser et al, 2004).

Legend:

full lines the numerical grid

grey area items with the same grid indices (M, N)

\+ water level, concentration of constituents, salinity, temperature

− horizontal velocity component in ξ-direction (also called u- and m-direction)

| horizontal velocity component in η-direction (also called v- and n-direction)

• depth below mean (still) water level (reference level)
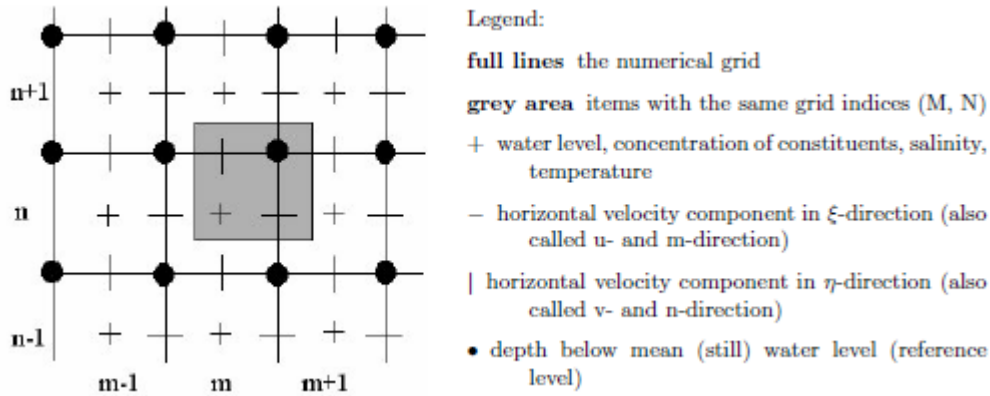
Figure 14-3 – Staggered grid (Deltares, 2009).
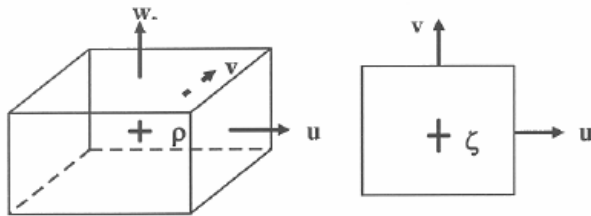
Legend:

\+ water level (ζ) / density (ρ) point

→ velocity point (u, v, or w)

Figure 14-4 – Grid staggering, 3D view (left) and top view (right) (Deltares, 2009).

15 Appendix 3 – Figures results sensitivity analysis on bed shear stress patterns
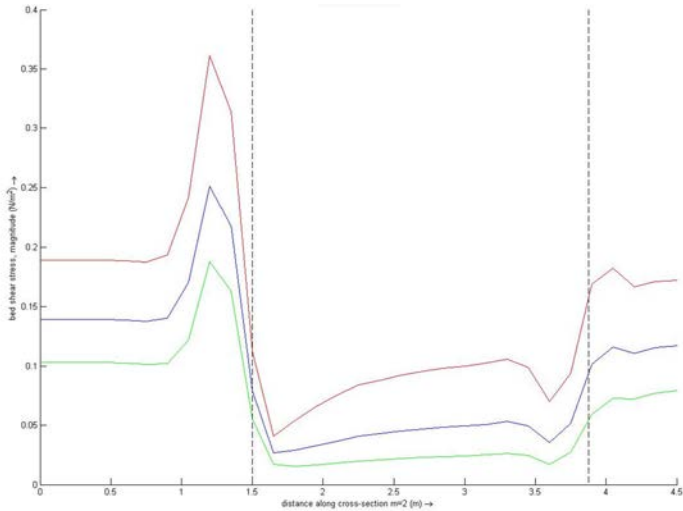
Figure 15-1 – Bed shear stress (N/m^2) in the x-direction with a density D of 2448 ind./m^2, a flow velocity u 0.2 m/s and a Chézy coefficient of 52, 65 and 78 m$^{1/2}$/s (red, blue and green line, respectively).The dashed lines indicate the patch of worms.
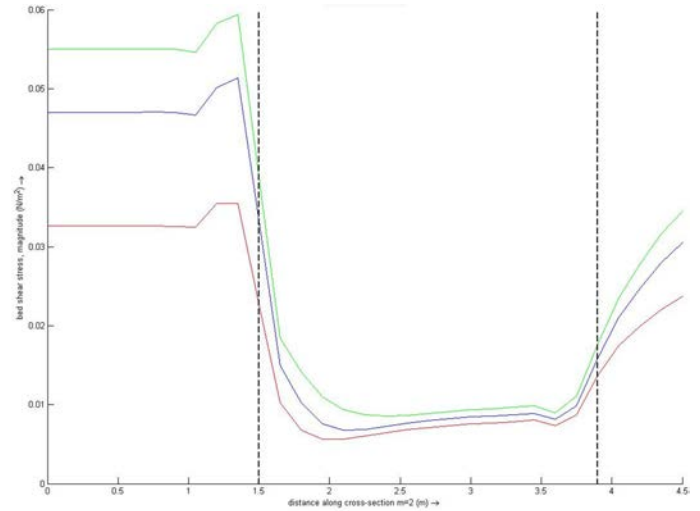
Figure 15-2 – Bed shear stress (N/m^2) in the x-direction with a density D of 2448 ind./m^2, a flow velocity u 0.2 m/s and a background vertical eddy viscosity of 80, 100 and 120 .10^{-6} m^2/s (red, blue and green line, respectively). The dashed lines indicate the patch of worms.
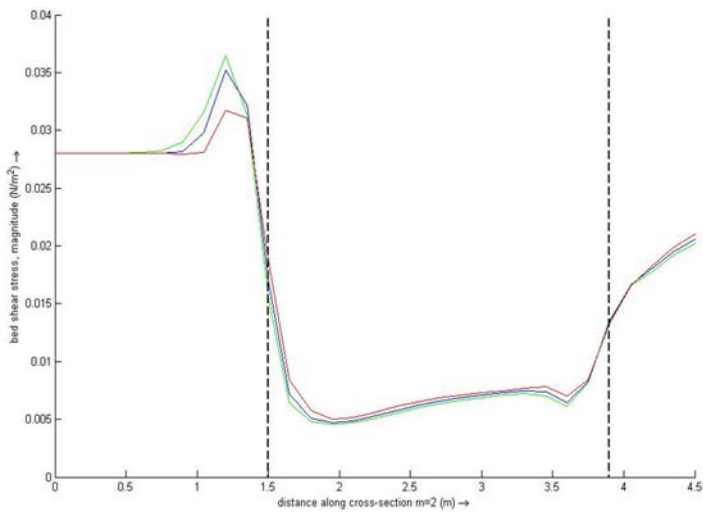
Figure 15-3 – Bed shear stress (N/m^2) in the x-direction with a density D of 2448 ind./m^2, a flow velocity u 0.2 m/s and a background horizontal eddy viscosity of 80, 100 and 120 .10^{-6} m^2/s (red, blue and green line, respectively). The dashed lines indicate the patch of worms.